A one-step Bayesian inversion framework for three-dimensional reservoir characterization based on a Gaussian mixture model – A Norwegian Sea demonstration

Torstein Fjeldstad[1], **Per Avseth**[2], **and Henning Omre**[3]

[1]*Department of Mathematical Sciences,*

Norwegian University of Science and Technology

E-mail: torstein.fjeldstad@ntnu.no

[2]*Department of Geoscience and Petroleum,*

Norwegian University of Science and Technology

E-mail: per.aage.avseth@gmail.com

[3]*Department of Mathematical Sciences,*

Norwegian University of Science and Technology

E-mail: henning.omre@ntnu.no

(November 9, 2020)

Running head: **One-step Bayesian inversion**

ABSTRACT

A one-step approach for Bayesian prediction and uncertainty quantification of lithology/fluid classes, petrophysical properties and elastic attributes conditional on prestack 3D seismic amplitude-versus-offset data is presented. A 3D Markov random field prior model is assumed for the lithology/fluid classes to ensure spatially coupled lithology/fluid class predictions in both the lateral and vertical directions. Conditional on the lithology/fluid classes, we consider Gauss-linear petrophysical and rock physics models including depth trends. Then, the marginal prior models for the petrophysical properties and elastic attributes are multivariate Gaussian mixture models. The likelihood model is assumed to be Gauss-linear to allow for analytic computation. A recursive algorithm that translates the Gibbs formulation of the Markov random field into a set of vertical Markov chains is proposed. This algorithm provides a proposal density in a Markov chain Monte Carlo algorithm such that efficient simulation from the posterior model of interest in three dimensions is feasible. The model is demonstrated on real data from a Norwegian Sea gas reservoir. We evaluate the model at the location of a blind well, and we compare results from the proposed model with results from a set of 1D models where each vertical trace is inverted independently. At the blind well location, we obtain at most a 60 % reduction in the root mean square error for the proposed 3D model compared to the model without lateral spatial coupling.

INTRODUCTION

Quantitative interpretation (Avseth et al., 2005) of prestack seismic data is an essential part of the workflow both during prospect de-risking (exploration) and reservoir characterization (production) in the oil and gas industry to predict the proportion of hydrocarbon and to determine the well design for production. The objective is to reduce the technological and economic risk during the development phase. In reservoir characterization, there are three inverse problems (Tarantola, 2005): prediction of elastic attributes, such as P-impedance (elastic seismic inversion); prediction of rock and fluid properties, such as porosity and water saturation (petrophysical seismic inversion); and prediction of the lithology/fluid classes or facies (lithology/fluid classification). We refer to Grana et al. (2017) and references therein for a discussion of these inverse problems. Assessment of such geophysical inverse problems is a challenging task due to the uncertainty in the measurements and nonuniqueness of the solution. There are several sources of uncertainty in the workflow, including observation errors, limited bandwidth of seismic data and rock physics modeling errors. We refer to Bosch et al. (2010) for an overview of elastic seismic inversion.

Various deterministic (Aster et al., 2005; Sen and Stoffa, 2013) and probabilistic (Doyen, 1988; Lia et al., 1997; Tarantola, 2005) approaches exist to solve the abovementioned inverse problems. These approaches were first applied to elastic seismic inversion but have lately been extended to also cover petrophysical seismic inversion (Doyen, 2007). Deterministic techniques are often based on optimization of a misfit function including a penalty term for

regularization of the solution. In a Bayesian setting, a prior probability model is assigned to the reservoir variables of interest in order to include prior knowledge and experience. Probabilistic approaches have been applied successfully for reservoir characterization; see, e.g., Doyen (1988); Lia et al. (1997); Mukerji et al. (2001); Buland and Omre (2003); Gunning and Glinsky (2007); Rimstad and Omre (2010); Grana and Della Rossa (2010); Rimstad et al. (2012); Jullum and Kolbjørnsen (2016) and Connolly and Hughes (2016).

We consider a Bayesian framework where the solution is not only a point prediction but rather the full posterior model for the variables of interest, which allows for uncertainty and risk quantification. The posterior model is computed by combining the likelihood for the observed data given the reservoir variables and the prior model for the latter. In general, the class of models that can be solved analytically is limited, and sampling-based methods such as Markov chain Monte Carlo (Gamerman and Lopes, 2006) have to be applied. In sampling-based methods, an ensemble of realizations represent the posterior model, on which summary statistics and predictions are based. However, construction of a satisfactory proposal density in the simulation algorithm that ensures sufficiently fast convergence is challenging in high-dimensional problems.

Traditionally, Bayesian inversion techniques are based on a stepwise procedure, where one first inverts for the elastic attributes (Doyen, 2007), then for the petrophysical properties and finally for the lithology/fluid classes. These methodologies are often applied at the pointwise level, where lateral spatial continuity in the predictions is inferred only

from the spatial continuity of the seismic data. During the last decade, simultaneous (or joint/integrated/one-step) inversion techniques have been developed (Rimstad and Omre, 2010), and they capture the joint model and tend to represent the uncertainty more realistically. We consider the latter approach, where we jointly assess the posterior model of the variables of interest.

For a linear seismic model with an additive Gaussian error term and a Gaussian prior model for the elastic attributes, the posterior model for the elastic attributes is also Gaussian, with analytic expressions for the mean vector and covariance matrix (Buland and Omre, 2003). Pointwise classification of the lithology/fluid classes based on classification techniques, such as discriminant analysis (Hastie et al., 2009) or other machine learning techniques, may then be applied to obtain a lithology/fluid classification. The prior model has recently been extended to also cover Gaussian mixture prior models (Grana and Della Rossa, 2010; Grana et al., 2017) to model multimodal and skewed marginal characteristics, and we consider the latter class of models.

Spatial histograms of well logs for the petrophysical properties, such as porosity and water saturation, often appear as multimodal and/or skewed due to varying lithology classes and fluid fillings of the subsurface. We therefore include a lithology/fluid class variable to model these variations, as they have an important impact on the petrophysical properties. To honor vertical sorting and ordering of the lithology/fluid classes, Markov chain prior models are frequently used. The usage of Markov chains to model a vertical profile dates

back to Krumbein and Dacey (1969). These models are either used only for one-dimensional problems (Eidsvik et al., 2004; Connolly and Hughes, 2016; Fjeldstad and Omre, 2020) or used in coupling of vertical Markov chains in a 2D and 3D random field context (Rimstad and Omre, 2010; Ulvmoen and Omre, 2010; Fjeldstad and Grana, 2018; de Figueiredo et al., 2019). We extend this work by replacing the one-dimensional Markov chain prior model for the lithology/fluid classes with a three-dimensional Markov random random field prior model, which allows for consistent three-dimensional modeling. We refer to Kemper and Gunning (2014) and Gunning and Sams (2018) for more information regarding the use of Markov random fields in reservoir characterization. The main advantage of phrasing a full 3D model is that each posterior realization in a vertical trace borrows predictive power from its neighboring traces. Hence, posterior realizations are expected to have larger lateral spatial continuity. If the ultimate objective is to forecast reservoir productions, reproducing lateral connectivity is of the utmost importance. We refer to Tjelmeland et al. (2019) for a discussion of the impact of lateral continuity in lithology/fluid class prediction related to fluid flow.

Rock physics models relate the rock and fluid properties to the elastic attributes, and these relations are generally known for conventional reservoirs (Avseth et al., 2005; Mavko et al., 2009). Houck (2002) contains a discussion regarding the importance of considering both seismic and rock physics uncertainties, and in Bachrach (2006), stochastic rock physics models for joint prediction of porosity and saturation are presented. We consider the

class of Gauss-linear models conditional on the lithology/fluid classes and the petrophysical properties and elastic attributes, where the forward model is assumed to be linear in the reservoir variable together with an additive zero-mean Gaussian error term.

The ultimate objective is to assess the reservoir variables of interest given seismic amplitude-versus-offset (AVO) data. We use a Markov chain Monte Carlo Metropolis-Hastings algorithm to generate realizations from the correct posterior model of interest. Each iteration in the Metropolis-Hastings algorithm consists of two main steps: proposal of a new realization and accepting or rejecting the proposed sample. In high-dimensional problems, such as in reservoir characterization, the major challenge is to construct a reasonable proposal density in order to obtain satisfactory acceptance and convergence rates. Our focus is on construction of the proposal density in three dimensions, extending Rimstad and Omre (2013) and Fjeldstad and Omre (2020), and hence improving the convergence rate of the algorithm.

The main contribution of this paper is an algorithm that rephrases the complete Markov random field model in three dimensions into the set of corresponding conditional one-dimensional vertical Markov chain models. We present an efficient block-Gibbs algorithm in three dimensions based on analytic evaluations that may be used for sequential simulation. First, we define the probabilistic model in a Bayesian inversion setting and discuss assessment of the posterior model. Second, we demonstrate the methodology on a real Norwegian Sea case study. We consider seismic AVO data and refer to Avseth et al. (2016)

for details of the reservoir. The results are validated at the location of a blind well and compared to an alternative model based on a collection of 1D models, where each vertical profile is assumed to be independent of the other profiles.

MODEL DESCRIPTION

In the following section, we define the variables of interest and the probabilistic model, extending Fjeldstad and Grana (2018).

Notation

Denote by $p(\cdot)$ an arbitrary probability density/mass function (pdf). Vectors are given in lowercase bold font and matrices in uppercase bold font. Let $\mathcal{N}(\mathbf{x}; \boldsymbol{\mu}, \boldsymbol{\Sigma})$ denote the (multivariate) Gaussian pdf for a random vector $\mathbf{x}$ having mean vector $\boldsymbol{\mu}$ and covariance matrix $\boldsymbol{\Sigma}$. We refer to a likelihood model as Gauss-linear if the modeling variable is linear in the conditioning variable together with an additive Gaussian error term. Let $\mathbb{R}_{[a,b]}$ denote the set of real numbers on the interval $[a, b]$, where $a < b$ are real numbers.

Consider a discretized grid of the subsurface, $\mathcal{L} = \big\{(x, y, t) : x = 1, \ldots, n_x; y = 1, \ldots, n_y; \quad t = 1, \ldots, n_t\big\}$, where x and y are the coordinates in the horizontal direction and t is the vertical position (e.g., time) indexed top-down, and let $n = n_x n_y n_t$ denote the total number of grid cells in the cube. Let $v = xyt \in \mathcal{L}$ denote an arbitrary cell and $-v$ denote all cells except v. Moreover, denote

by $\mathcal{L}_{xy\cdot} = \{(x, y, t) : x, y, t = 1, \ldots, n_t\} \subset \mathcal{L}$ the set of vertical nodes at horizontal position xy and let $\mathcal{L}_{-xy\cdot} = \mathcal{L} \setminus \mathcal{L}_{xy\cdot}$, where $\setminus$ denotes the set difference. Finally, let $\mathbf{u} = (xy1, \ldots, xyn_t) \subset \mathcal{L}$ denote the indices of a full vertical profile at horizontal position xy.

The variables of interest on the grid $\mathcal{L}$ are the lithology/fluid classes $\boldsymbol{\kappa} = (\kappa_1, \ldots, \kappa_n)$, the petrophysical properties $\mathbf{r} = (r_1, \ldots, r_n)$ and the logarithm of the elastic attributes $\mathbf{m} = (m_1, \ldots, m_n)$. Moreover, let $r_v \in \Omega_r = \mathbb{R}_{[0,1]}$ and $m_v \in \Omega_m = \mathbb{R}_{[0,\infty)}$ denote the petrophysical property, taking on values on $[0, 1]$, and the elastic attribute, which takes positive values, respectively. Since rock properties such as the porosity, water saturation, permeability and net-to-gross are bounded on $\mathbb{R}^n_{[0,1]}$, we use an elementwise logit-transformation to ensure support on $\mathbb{R}^n$. The logit-transform is one-to-one, which ensures that we can transform back to the original domain.

To ease notation, we specify in the following the probabilistic model only for one petrophysical property variable (porosity) and one elastic attribute variable (logarithm of P-impedance) at each grid cell $v \in \mathcal{L}$. The proposed methodology is valid for additional petrophysical properties and elastic attributes such as water saturation and/or the logarithm of the Poisson ratio at the expense of a more complex notation. Each node $v \in \mathcal{L}$ is assigned three stochastic variables κ_v, r_v and m_v. Let $\kappa_v \in \Omega_\kappa = \{1, \ldots, L\}$; hence, κ_v takes one out of L categorial values in each grid cell. These categorical values represent the lithology/fluid classes of the subsurface, for example, gas sandstone or shale. We consider

prestack seismic amplitude-versus-offset (AVO) data $\mathbf{d} = (d_1, \ldots, d_n)$ and consider only one incidence angle in the following to ease notation. We refer to Buland and Omre (2003) for an extension to multiple incident angles. A short description of the variables to be defined is given Table 1.

Bayesian inversion

Recall that the variables of interest are the lithology/fluid classes $\boldsymbol{\kappa}$, the petrophysical properties $\mathbf{r}$ and the logarithm of the elastic attributes $\mathbf{m}$ of the subsurface. The objective is to characterize these variables given seismic AVO data in a joint spatial Bayesian inverse setting. A one-step joint methodology allows for a consistent treatment of the uncertainties, as these uncertainties are often underestimated in a stepwise procedure.

We operate in a Bayesian inversion framework, where the ultimate objective is to assess the joint posterior pdf of the variables of interest; that is,

$$\begin{aligned} p\big(\boldsymbol{\kappa}, \mathbf{r}, \mathbf{m} \mid \mathbf{d}\big) &\propto p\big(\mathbf{d} \mid \boldsymbol{\kappa}, \mathbf{r}, \mathbf{m}\big) p(\boldsymbol{\kappa}, \mathbf{r}, \mathbf{m}) \\ &= p\big(\mathbf{d} \mid \mathbf{m}\big) p\big(\mathbf{m} \mid \boldsymbol{\kappa}, \mathbf{r}\big) p\big(\mathbf{r} \mid \boldsymbol{\kappa}\big) p(\boldsymbol{\kappa}) \end{aligned} \tag{1}$$

since $\mathbf{m}$ is a canonical variable for $\mathbf{d}$. We refer to the likelihood model $p\big(\mathbf{d} \mid \mathbf{m}\big)$ as the seismic model. The joint prior model $p(\boldsymbol{\kappa}, \mathbf{r}, \mathbf{m})$ is sequentially decomposed, and we refer to $p(\boldsymbol{\kappa})$ as the lithology/fluid class model, $p\big(\mathbf{r} \mid \boldsymbol{\kappa}\big)$ as the petrophysical model and $p\big(\mathbf{m} \mid \boldsymbol{\kappa}, \mathbf{r}\big)$ as the rock physics model. The latter two models are defined conditional on the lithology/fluid classes $\boldsymbol{\kappa}$. Obtaining the normalizing constant of equation (1) may not be computationally

feasible since it requires a summation over $\boldsymbol{\kappa} \in \Omega_{\kappa}^{n}$ and evaluation of the high-dimensional integral over $\mathbf{r}$ and $\mathbf{m}$ to obtain the normalizing constant $p(\mathbf{d})$.

We assume the petrophysical model, rock physics model and likelihood model to have the factorial form

$$p\big(\boldsymbol{\kappa}, \mathbf{r}, \mathbf{m} \mid \mathbf{d}\big) \propto \prod_{\mathbf{u}=1}^{n_x n_y} \Big[p\big(\mathbf{d_u} \mid \mathbf{m_u}\big) p\big(\mathbf{m_u} \mid \boldsymbol{\kappa_u}, \mathbf{r_u}\big) p\big(\mathbf{r_u} \mid \boldsymbol{\kappa_u}\big)\Big] \times p(\boldsymbol{\kappa}), \tag{2}$$

Hence, the observations $\mathbf{d_u}$ for each vertical trace are conditionally independent of the observations for every other vertical trace given $\boldsymbol{\kappa}$. Note that the sequential decomposition of the prior model above does not imply that the joint prior density $p(\boldsymbol{\kappa}, \mathbf{r}, \mathbf{m})$ can be factored into a set of vertical independent prior densities. That is, even if the conditional density $p\big(\mathbf{r}, \mathbf{m} \mid \boldsymbol{\kappa}\big)$ is laterally independent, the unconditional density $p(\mathbf{r}, \mathbf{m}) = \sum_{\boldsymbol{\kappa}} p\big(\mathbf{r}, \mathbf{m} \mid \boldsymbol{\kappa}\big) p(\boldsymbol{\kappa})$ is laterally correlated. Next, we define the petrophysical model, rock physics model and likelihood model for each vertical profile $\mathbf{u}$.

Likelihood model

The observed seismic signal d_v at grid cell $v = xyt \in \mathcal{L}$ can be represented as a convolution of the reflection coefficients along the vertical profile $\mathcal{L}_{xy\cdot}$ and a wavelet due to the reflection and transmission of the seismic waves in the subsurface.

Seismic model

We consider a linearized approximation of the nonlinear Zoeppritz equations based on the Aki-Richards formulation for weak contrasts (Aki and Richards, 1980) following Buland and Omre (2003). We assume a Gauss-linear likelihood model

$$p(\mathbf{d_u} \mid \mathbf{m_u}) = \mathcal{N}\left(\mathbf{d_u}; \mathbf{G}\mathbf{m_u}, \mathbf{\Sigma_{d_u}}\right); \tag{3}$$

that is, the model is linear in the conditioning variable $\mathbf{m}$ with additive Gaussian error terms. The linear operator $\mathbf{G}$ is a $(n_t \times n_t)$-matrix assumed to be the product of three matrices $\mathbf{G} = \mathbf{WAD}$ (Buland and Omre, 2003), where $\mathbf{W}$ is the $(n_t \times n_t)$ convolution matrix, $\mathbf{A}$ is a $(n_t \times n_t)$-matrix containing the angle dependent Aki-Richards reflection coefficients and $\mathbf{D}$ is a $(n_t \times n_t)$-matrix approximating derivative. We assume that the $(n_t \times n_t)$-covariance matrix $\mathbf{\Sigma_{d_u}}$ includes vertically colored noise.

Prior model

The prior model in equation (2) is specified sequentially, as in Fjeldstad and Grana (2018), and we discuss the lithology/fluid class, petrophysical property and elastic attributes models separately.

Lithology/fluid class model

To model the spatial connectivity and continuity of the lithology/fluid classes $\boldsymbol{\kappa}$, we consider a Markov random field model (Besag, 1974), which requires some additional notation. We consider the set of cliques $c \subset \mathcal{L}$, which consists of the pairs of closest neighbors. Let $\mathcal{C}$ denote the clique system that is the set of all cliques. Let $n_v \in \mathcal{L}$ be the set of neighbors of each $v \in \mathcal{L}$. Given the clique system of the closest pairwise cliques, it follows that n_v consists of the six closest neighbors, not including v itself, for each $v \in \mathcal{L}$. A stencil of the neighborhood system is given in Figure 1. The methodology presented is also valid for a more complex clique set, at the expense of a more complex notation. We phrase the lithology/fluid prior model in Gibbs form (Kemper and Gunning, 2014; Gunning and Sams, 2018):

$$p(\boldsymbol{\kappa}) = \text{const}_1^{-1} \times \exp\left(-\sum_{c \in \mathcal{C}} g_c(\boldsymbol{\kappa}_c)\right), \tag{4}$$

where each $g_c(\cdot)$ is a real-valued function. The normalizing constant in equation (4), $\text{const}_1 = \sum_{\boldsymbol{\kappa}' \in \Omega_\kappa^n} \exp\left(-\sum_{c \in \mathcal{C}} g_c(\boldsymbol{\kappa}'_c)\right)$, is in general not analytically tractable, as it requires summation over $\boldsymbol{\kappa} \in \Omega_\kappa^n$, which has L^n elements.

The locationwise (conditional) Markov formulation is given as

$$\begin{aligned} p\left(\kappa_v \mid \boldsymbol{\kappa}_{-v}\right) &\propto \exp\left(-\sum_{w \in n_v} g_c\left(\kappa_v, \boldsymbol{\kappa}_w\right)\right) \\ &= \text{const}_2^{-1} \times \exp\left(-h_v(\kappa_v \mid \kappa_w; w \in n_v)\right) \end{aligned} \tag{5}$$

where $h_v(\cdot)$ is a real-valued function defined by the Gibbs formulation and neighborhood

system n_v to account for heterogeneities. The normalizing constant is given by $\text{const}_2 = \sum_{\kappa'_v \in \Omega_\kappa} \exp\big(-h_v(\kappa'_v \mid \kappa_w; w \in n_v)\big)$, which is feasible to compute since it only requires a sum over $\kappa_v \in \Omega_\kappa$. The restriction $v \in c$ in equation (5) implies that we need only consider the set of cliques associated with neighborhood n_v. Hence, the pdf including the normalizing constant is computationally tractable. Simulation from the prior $p(\boldsymbol{\kappa})$ defined in equation (4) is often performed by Markov chain Monte Carlo simulation using the set of full-conditional pdfs $p\big(\kappa_v \mid \boldsymbol{\kappa}_{-v}\big)$ in equation (5) for each $v \in \mathcal{L}$.

We consider a block-update Gibbs scheme where a subset of nodes is updated at each iteration. A joint update scheme for each vertical trace $\mathbf{u}$ is proposed. We rephrase the conditional pdf for each trace in sequential form as a vertical Markov chain:

$$\begin{aligned} p\big(\boldsymbol{\kappa}_{xy\cdot} \mid \boldsymbol{\kappa}_{-xy\cdot}\big) &= \prod_{t=1}^{n_t} p\Big(\kappa_{xyt} \mid \boldsymbol{\kappa}_{xy,1:(t-1)}, \boldsymbol{\kappa}_{-xy\cdot}\Big) \\ &= \prod_{t=1}^{n_t} p\Big(\kappa_{xyt} \mid \kappa_{xy,(t-1)}, \boldsymbol{\kappa}_{-xy\cdot}\Big) \end{aligned}, \tag{6}$$

where $p\big(\kappa_{xy1} \mid \kappa_{xy0}, \boldsymbol{\kappa}_{-xy\cdot}\big) = p\big(\kappa_{xy1} \mid \boldsymbol{\kappa}_{-xy\cdot}\big)$ to ease notation. The latter equality of equation (6) follows from the simpler first order neighborhood n_v. We propose a recursive algorithm to obtain the set of conditional pdfs $p\Big(\kappa_{xyt} \mid \kappa_{xy,(t-1)}, \boldsymbol{\kappa}_{-xy\cdot}\Big)$.

We observe that $p\Big(\kappa_{xy,n_t} \mid \kappa_{xy,(n_t-1)}, \boldsymbol{\kappa}_{-xy\cdot}\Big)$ is available directly from the locationwise Markov formulation in equation (5). The locationwise Markov formulation for $t = n_t - 1, \ldots, 2$ is given as

$$\begin{aligned} p\big(\kappa_{xyt} \mid \boldsymbol{\kappa}_{-xyt}\big) &\propto p\Big(\kappa_{xyt} \mid \boldsymbol{\kappa}_{xy,1:(t-1)}, \boldsymbol{\kappa}_{-xy\cdot}\Big) \prod_{t'=t}^{n_t-1} p\Big(\kappa_{xy,(t'+1)} \mid \boldsymbol{\kappa}_{xy,1:t'}, \boldsymbol{\kappa}_{-xy\cdot}\Big) \\ &\propto p\Big(\kappa_{xyt} \mid \kappa_{xy,(t-1)}, \boldsymbol{\kappa}_{-xy\cdot}\Big) p\Big(\kappa_{xy,(t+1)} \mid \kappa_{xyt}, \boldsymbol{\kappa}_{-xy\cdot}\Big) \end{aligned}. \tag{7}$$

By rephrasing equation (7), we obtain

$$p\Big(\kappa_{xyt} \mid \kappa_{xy,(t-1)}, \boldsymbol{\kappa}_{-xy\cdot}\Big) \propto \frac{p\big(\kappa_{xyt} \mid \boldsymbol{\kappa}_{-xyt}\big)}{p\Big(\kappa_{xy,(t+1)} \mid \kappa_{xyt}, \boldsymbol{\kappa}_{-xy\cdot}\Big)}. \tag{8}$$

The normalizing constant is tractable since it is a sum over $\kappa \in \Omega_\kappa$, which is feasible to compute. Since each pdf $p\Big(\kappa_{xyt} \mid \kappa_{xy,(t-1)}, \boldsymbol{\kappa}_{-xy\cdot}\Big)$ depends only on $p\big(\kappa_{xyt} \mid \boldsymbol{\kappa}_{-xyt}\big)$ and the previous iteration $p\Big(\kappa_{xy,(t+1)} \mid \kappa_{xyt}, \boldsymbol{\kappa}_{-xy\cdot}\Big)$, one may use a recursive algorithm to obtain the transition probabilities in equation (6) by iterating downwards $t = n_t - 1, \ldots, 2$. Finally, for $t = 1$, we obtain

$$p\big(\kappa_{xy1} \mid \boldsymbol{\kappa}_{-xy\cdot}\big) \propto \frac{p\big(\kappa_{xy1} \mid \boldsymbol{\kappa}_{-xy1}\big)}{p\big(\kappa_{xy2} \mid \kappa_{xy1}, \boldsymbol{\kappa}_{-xy\cdot}\big)}. \tag{9}$$

The resulting recursive algorithm is given in Algorithm 1.

Petrophysical model

Recall that we operate in the logit-domain for the petrophysical properties; however, to ease notation we will refer to $\text{logit}(\mathbf{r})$ as $\mathbf{r}$. We assume the petrophysical model (in logit-domain) to be Gaussian,

$$p\big(\mathbf{r_u} \mid \boldsymbol{\kappa_u}\big) = \mathcal{N}\left(\mathbf{r_u}; \boldsymbol{\mu}_{\mathbf{r_u}|\boldsymbol{\kappa_u}}, \boldsymbol{\Sigma}_{\mathbf{r_u}|\boldsymbol{\kappa_u}}\right), \tag{10}$$

with conditional n_t-mean-vector $\boldsymbol{\mu}_{\mathbf{r_u}|\boldsymbol{\kappa_u}} = \left(\mu_{r_{xy1}|\kappa_{xy1}}, \ldots, \mu_{r_{xyn_t}|\kappa_{xyn_t}}\right)$ and $(n_t \times n_t)$-covariance matrix $\boldsymbol{\Sigma}_{\mathbf{r_u}|\boldsymbol{\kappa_u}}$. The pointwise expected value $\mu_{r_{xyt}|\kappa_{xyt}}$ takes on one of L distinct values dependent on the value of $\kappa_v \in \Omega_\kappa$ and might depend on v to model fixed lateral

Algorithm 1: Reverse algorithm for transition probabilities.

Result: Transition probabilities $\left\{p\Big(\kappa_{xyt} \mid \kappa_{xy,(t-1)}, \boldsymbol{\kappa}_{-xy\cdot}\Big)\right\}$

$p\Big(\kappa_{xyn_t} \mid \kappa_{xy,(n_t-1)}, \boldsymbol{\kappa}_{-xy\cdot}\Big) = p\big(\kappa_{xyn_t} \mid \boldsymbol{\kappa}_{-xyn_t}\big)$

for $t = n_t - 1$ **to** 2 **do**

  $p\Big(\kappa_{xyt} \mid \kappa_{xy,(t-1)}, \boldsymbol{\kappa}_{-xy\cdot}\Big) = \text{const} \times \frac{p\left(\kappa_{xyt} \mid \boldsymbol{\kappa}_{-xyt}\right)}{p\left(\kappa_{xy,(t+1)} \mid \kappa_{xyt}, \boldsymbol{\kappa}_{-xy\cdot}\right)}$

  $\text{const}^{-1} = \sum_{\kappa'_{xyt} \in \Omega_\kappa} p\Big(\kappa'_{xyt} \mid \kappa_{xy,(t-1)}, \boldsymbol{\kappa}_{-xy\cdot}\Big)$

end

$p\big(\kappa_{xy1} \mid \boldsymbol{\kappa}_{-xy\cdot}\big) = \text{const} \times \frac{p\left(\kappa_{xy1} \mid \boldsymbol{\kappa}_{-xy1}\right)}{p\left(\kappa_{xy2} \mid \kappa_{xy1}, \boldsymbol{\kappa}_{-xy\cdot}\right)}$

$\text{const}^{-1} = \sum_{\kappa'_{xy1}} p\Big(\kappa'_{xy1} \mid \boldsymbol{\kappa}_{-xy\cdot}\Big)$

return $\left\{p\Big(\kappa_{xyt} \mid \kappa_{xy,(t-1)}, \boldsymbol{\kappa}_{-xy\cdot}\Big)\right\}$.

and vertical trends such as compaction.

It can be demonstrated that the marginal multivariate pdf for the petrophysical properties is a spatially coupled Gaussian mixture pdf (see Fjeldstad and Omre (2020) and references therein):

$$p(\mathbf{r}) = \sum_{\boldsymbol{\kappa} \in \Omega_\kappa^n} p\big(\mathbf{r} \mid \boldsymbol{\kappa}\big) p(\boldsymbol{\kappa}). \tag{11}$$

That is, each univariate marginal pdf $p(r_v)$ is a Gaussian mixture pdf that can be used to model skewness and multimodality a priori to represent various lithology effects. Since $\boldsymbol{\kappa}$ is assigned a Markov random field prior model with both lateral and vertical spatial dependency, $p(\mathbf{r})$ includes both spatial and vertical correlation.

Rock physics model

Rock physics models are in general nonlinear but can be locally linearized (Landrø, 2001; Grana, 2016) or empirically fitted. We consider a probabilistic Gaussian lithology/fluid class-dependent rock physics model to represent various lithology/fluid and petrophysical effects:

$$p(\mathbf{m_u} \mid \boldsymbol{\kappa_u}, \mathbf{r_u}) = \mathcal{N}\left(\mathbf{m_u}; \boldsymbol{\mu}_{\mathbf{m_u}|\boldsymbol{\kappa_u}} + \mathbf{B}_{\boldsymbol{\kappa_u}}\mathbf{r_u}, \boldsymbol{\Sigma}_{\mathbf{m_u}|\boldsymbol{\kappa_u}}\right), \tag{12}$$

where $\boldsymbol{\mu}_{\mathbf{m_u}|\boldsymbol{\kappa_u}} = \left(\mu_{m_{xy1}|\kappa_{xy1}}, \ldots, \mu_{m_{xyn_t}|\kappa_{xyn_t}}\right)$ is the n_t-vector of pointwise expected values for the elastic attributes similar as $\boldsymbol{\mu}_{\mathbf{r_u}|\boldsymbol{\kappa_u}}$, $\mathbf{B}_{\boldsymbol{\kappa_u}}$ is a $(n_t \times n_t)$-block-diagonal matrix with lithology/fluid class dependent coefficients, and $\boldsymbol{\Sigma}_{\mathbf{m_u}|\boldsymbol{\kappa_u}}$ is an $(n_t \times n_t)$-covariance matrix with colored noise. As for the petrophysical model, it is possible to include fixed depth-trends in the rock physics model for each lithology/fluid class which makes the full rock-physics model nonlinear.

The multivariate marginal pdf for the elastic attributes is a Gaussian mixture pdf:

$$p(\mathbf{m}) = \sum_{\boldsymbol{\kappa} \in \Omega_\kappa^n} \int p(\mathbf{m} \mid \boldsymbol{\kappa}, \mathbf{r}) p(\mathbf{r} \mid \boldsymbol{\kappa}) \mathrm{d}\mathbf{r} \times p(\boldsymbol{\kappa}) = \sum_{\boldsymbol{\kappa} \in \Omega_\kappa^n} p(\mathbf{m} \mid \boldsymbol{\kappa}) \times p(\boldsymbol{\kappa}). \tag{13}$$

We interpret the marginal rock physics model as a nonlinear model, where the model itself assigns the rock physics model marginally depending on the corresponding lithology/fluid class. Note that a Gauss-linear lithology/fluid class dependent rock physics model based on the logit-transform implies that the lithology/fluid class dependent rock physics model in the original domain is nonlinear. Since the mixing weights $p(\boldsymbol{\kappa})$ includes both vertical

and horizontal lateral dependency, $p(\mathbf{m})$ includes both vertical and horizontal coupling.

Posterior model

We present a block-Gibbs simulation algorithm to assess the joint posterior $p\big(\boldsymbol{\kappa}, \mathbf{r}, \mathbf{m} \mid \mathbf{d}\big)$ with a block update of the full vertical trace at horizontal position xy in each iteration. In general, the Markov chain Monte Carlo Metropolis-Hastings algorithm consists of two steps. First, there is a proposal step where a trace of updated variables is proposed, and then, there is an accept-or-reject step where this trace is accepted with a certain probability. We discuss both parts in detail. Finally, we relate the proposed simulation algorithm to strategies proposed earlier.

First, initialize $\boldsymbol{\kappa}, \mathbf{r}$ and $\mathbf{m}$ with $p\big(\boldsymbol{\kappa}, \mathbf{r}, \mathbf{m} \mid \mathbf{d}\big) > 0$, denote by superscript i the current value of $\boldsymbol{\kappa}, \mathbf{r}$ and $\mathbf{m}$, and consider a random vertical trace $\mathbf{u}$. The proposed workflow consist of the following steps:

Proposal step: In each iteration, we consider the following block-dependent proposal density:

$$\begin{aligned} q\left(\boldsymbol{\kappa}_{\mathbf{u}}, \mathbf{r}_{\mathbf{u}}, \mathbf{m}_{\mathbf{u}} \mid \boldsymbol{\kappa}^{i}_{-\mathbf{u}}, \mathbf{r}^{i}_{-\mathbf{u}}, \mathbf{m}^{i}_{-\mathbf{u}}, \mathbf{d}\right) \propto\; & q\left(\boldsymbol{\kappa}_{\mathbf{u}} \mid \boldsymbol{\kappa}^{i}_{-\mathbf{u}}, \mathbf{d}_{\mathbf{u}}\right) \\ & \times p\Big(\mathbf{r}_{\mathbf{u}} \mid \boldsymbol{\kappa}_{\mathbf{u}}, \boldsymbol{\kappa}^{i}_{-\mathbf{u}}, \mathbf{r}^{i}_{-\mathbf{u}}\Big) \\ & \times p\Big(\mathbf{m}_{\mathbf{u}} \mid \boldsymbol{\kappa}_{\mathbf{u}}, \mathbf{r}_{\mathbf{u}}, \boldsymbol{\kappa}^{i}_{-\mathbf{u}}, \mathbf{r}^{i}_{-\mathbf{u}}, \mathbf{m}^{i}_{-\mathbf{u}}\Big) \end{aligned} \quad . \tag{14}$$

To simulate from the block proposal density, we perform the following steps. First,

we construct the Markov chain $p(\boldsymbol{\kappa}_{\mathbf{u}} \mid \boldsymbol{\kappa}^i_{-\mathbf{u}})$ using the recursion defined in Algorithm 1. Because of the convolution, exact assessment of $p(\boldsymbol{\kappa}_{\mathbf{u}} \mid \boldsymbol{\kappa}_{-\mathbf{u}}, \mathbf{d}_{\mathbf{u}}) \propto p(\mathbf{d}_{\mathbf{u}} \mid \boldsymbol{\kappa}_{\mathbf{u}}) p(\boldsymbol{\kappa}_{\mathbf{u}} \mid \boldsymbol{\kappa}_{-\mathbf{u}})$ is unfeasible since it is a high-order Markov chain. We consider a k-th order Markov chain approximation $q(\boldsymbol{\kappa}_{\mathbf{u}} \mid \boldsymbol{\kappa}_{-\mathbf{u}}, \mathbf{d}_{\mathbf{u}})$ as in Fjeldstad and Omre (2020) based on a set of Gaussian approximations. The approximate pdf $q(\boldsymbol{\kappa}_{\mathbf{u}} \mid \boldsymbol{\kappa}_{-\mathbf{u}}, \mathbf{d}_{\mathbf{u}}) \propto \widetilde{p}(\mathbf{d}_{\mathbf{u}} \mid \boldsymbol{\kappa}_{\mathbf{u}}) p(\boldsymbol{\kappa}_{\mathbf{u}} \mid \boldsymbol{\kappa}^i_{-\mathbf{u}})$ is then exactly assessed by the recursive forward-backward algorithm (Reeves and Pettitt, 2004). Here, $\widetilde{p}(\mathbf{d}_{\mathbf{u}} \mid \boldsymbol{\kappa}_{\mathbf{u}})$ is an approximation to the exact likelihood model $p(\mathbf{d}_{\mathbf{u}} \mid \boldsymbol{\kappa}_{\mathbf{u}})$. Note that the algorithm presented in Algorithm 1 can be used directly to assess $q(\boldsymbol{\kappa}_{\mathbf{u}} \mid \boldsymbol{\kappa}_{-\mathbf{u}}, \mathbf{d}_{\mathbf{u}})$ by including a term dependent on $\mathbf{d}$, $\widetilde{p}(\mathbf{d}_{\mathbf{u}} \mid \boldsymbol{\kappa}_{\mathbf{u}})$, in equation (4). Because of the convolution, the simpler first-order neighborhood system is extended to a higher-order neighborhood system, and the algorithm has to be modified accordingly. Finally, we propose $\boldsymbol{\kappa}_{\mathbf{u}} \sim q(\boldsymbol{\kappa}_{\mathbf{u}} \mid \boldsymbol{\kappa}^i_{-\mathbf{u}}, \mathbf{d}_{\mathbf{u}})$, $\mathbf{r}_{\mathbf{u}} \sim p(\mathbf{r}_{\mathbf{u}} \mid \boldsymbol{\kappa}_{\mathbf{u}}, \boldsymbol{\kappa}^i_{-\mathbf{u}}, \mathbf{r}^i_{-\mathbf{u}})$ and $\mathbf{m}_{\mathbf{u}} \sim p(\mathbf{m}_{\mathbf{u}} \mid \boldsymbol{\kappa}_{\mathbf{u}}, \mathbf{r}_{\mathbf{u}}, \boldsymbol{\kappa}^i_{-\mathbf{u}}, \mathbf{r}^i_{-u}, \mathbf{m}^i_{-u})$. Here, laterally smooth realizations of $\mathbf{r}_u$ are constructed by assuming a joint multivariate Gaussian pdf for $\mathbf{r}_u$ and its four neighboring traces in $\mathbf{r}^i_{-\mathbf{u}}$ together with a spatial correlation coefficient ϱ_r, which acts as a spatial smoother or regularizer in the horizontal direction. Note that the marginal expectations and variances are specified from the petrophysical model; this implies that an analytic expression for $p(\mathbf{r}_{\mathbf{u}} \mid \boldsymbol{\kappa}_{\mathbf{u}}, \boldsymbol{\kappa}^i_{-\mathbf{u}}, \mathbf{r}^i_{-\mathbf{u}})$ is available. We construct $p(\mathbf{m}_{\mathbf{u}} \mid \boldsymbol{\kappa}_{\mathbf{u}}, \mathbf{r}_{\mathbf{u}}, \boldsymbol{\kappa}^i_{-\mathbf{u}}, \mathbf{r}^i_{-\mathbf{u}}, \mathbf{m}^i_{-\mathbf{u}})$ similarly by correlating the vertical profile $\mathbf{m}_{\mathbf{u}}$ with its four nearest neighboring traces in $\mathbf{m}^i_{-\mathbf{u}}$ by assuming a spatial correlation coefficient ϱ_m between neighboring vertical

traces to construct a joint pdf.

Accept/reject step: The proposed values of $\boldsymbol{\kappa}_{\mathbf{u}}, \mathbf{r}_{\mathbf{u}}$ and $\mathbf{m}_{\mathbf{u}}$ are accepted with probability

$$\alpha = \min \left\{ 1, \frac{p(\mathbf{d_u} \mid \mathbf{m_u}) p(\mathbf{m_u} \mid \boldsymbol{\kappa}_{\mathbf{u}}, \mathbf{r_u}) p(\mathbf{r_u} \mid \boldsymbol{\kappa}_{\mathbf{u}}) p(\boldsymbol{\kappa}_{\mathbf{u}} \mid \boldsymbol{\kappa}^i_{-\mathbf{u}})}{p(\mathbf{d_u} \mid \mathbf{m}^i_{\mathbf{u}}) p(\mathbf{m}^i_{\mathbf{u}} \mid \boldsymbol{\kappa}^i_{\mathbf{u}}, \mathbf{r}^i_{\mathbf{u}}) p(\mathbf{r}^i_{\mathbf{u}} \mid \boldsymbol{\kappa}^i_{\mathbf{u}}) p(\boldsymbol{\kappa}^i_{\mathbf{u}} \mid \boldsymbol{\kappa}^i_{-\mathbf{u}})} \right. \\ \left. \times \frac{\widetilde{p}\left(\mathbf{d_u} \mid \boldsymbol{\kappa}^i_{\mathbf{u}}\right) p(\boldsymbol{\kappa}^i_{\mathbf{u}} \mid \boldsymbol{\kappa}^i_{-\mathbf{u}}) p(\mathbf{r}^i_{\mathbf{u}} \mid \boldsymbol{\kappa}^i_{\mathbf{u}}, \boldsymbol{\kappa}^i_{-\mathbf{u}}, \mathbf{r}^i_{-\mathbf{u}}) p(\mathbf{m}^i_{\mathbf{u}} \mid \boldsymbol{\kappa}^i_{\mathbf{u}}, \mathbf{r}^i_{\mathbf{u}}, \boldsymbol{\kappa}^i_{-\mathbf{u}}, \mathbf{r}^i_{-\mathbf{u}}, \mathbf{m}^i_{-\mathbf{u}})}{\widetilde{p}\left(\mathbf{d_u} \mid \boldsymbol{\kappa}_{\mathbf{u}}\right) p(\boldsymbol{\kappa}_{\mathbf{u}} \mid \boldsymbol{\kappa}^i_{-\mathbf{u}}) p(\mathbf{r_u} \mid \boldsymbol{\kappa}_{\mathbf{u}}, \boldsymbol{\kappa}^i_{-\mathbf{u}}, \mathbf{r}^i_{-\mathbf{u}}) p(\mathbf{m_u} \mid \boldsymbol{\kappa}_{\mathbf{u}}, \mathbf{r_u}, \boldsymbol{\kappa}^i_{-\mathbf{u}}, \mathbf{r}^i_{-\mathbf{u}}, \mathbf{m}^i_{-\mathbf{u}})} \right\}. \tag{15}$$

These steps are performed until convergence, and the result is an ensemble of realizations from the posterior $p(\boldsymbol{\kappa}, \mathbf{r}, \mathbf{m} \mid \mathbf{d})$. After convergence, the realizations are combined to construct marginal summary statistics such as marginal probabilities for the lithology/fluid classes and marginal maximum a-posteriori (MMAP) predictors for the continuous-valued properties.

Alternative sampling strategies

The accept-or-reject step increases the computational complexity because it requires evaluation of a high-dimensional Gaussian pdf $p(\mathbf{d_u} \mid \boldsymbol{\kappa}_{\mathbf{u}})$. To reduce the computational complexity, one alternative is to omit the accept-or-reject step and only consider an approximate posterior solution $\tilde{p}\left(\boldsymbol{\kappa}, \mathbf{r}, \mathbf{m} \mid \mathbf{d}\right)$. An alternative is to consider an importance sampling algorithm (Gamerman and Lopes, 2006), where each proposed realization is assigned a corresponding importance weight $p\left(\boldsymbol{\kappa}_{\mathbf{u}}, \mathbf{r_u}, \mathbf{m_u} \mid \boldsymbol{\kappa}^i_{-\mathbf{u}}, \mathbf{r}^i_{-\mathbf{u}}, \mathbf{m}^i_{-\mathbf{u}}, \mathbf{d}\right) / q\left(\boldsymbol{\kappa}_{\mathbf{u}}, \mathbf{r_u}, \mathbf{m_u} \mid \boldsymbol{\kappa}^i_{-\mathbf{u}}, \mathbf{r}^i_{-\mathbf{u}}, \mathbf{m}^i_{-\mathbf{u}}, \mathbf{d}\right)$. If we propose $\mathbf{r_u} \sim p(\mathbf{r_u} \mid \boldsymbol{\kappa}_{\mathbf{u}})$ and $\mathbf{m_u} \sim p(\mathbf{m_u} \mid \boldsymbol{\kappa}_{\mathbf{u}}, \mathbf{r_u})$, the acceptance rate defined in equation (15) can be

further simplified to reduce the computational complexity (Rimstad and Omre, 2010). Another alternative is to also condition on $\mathbf{d_u}$ when proposing to update $\mathbf{r_u}$ and $\mathbf{m_u}$, that is, to simulate $\mathbf{r_u} \sim p\big(\mathbf{r_u} \mid \boldsymbol{\kappa_u}, \boldsymbol{\kappa}^i_{-\mathbf{u}}, \mathbf{r}^i_{-\mathbf{u}}, \mathbf{d_u}\big)$ and $\mathbf{m_u} \sim p\big(\mathbf{m_u} \mid \boldsymbol{\kappa_u}, \mathbf{r_u}, \boldsymbol{\kappa}^i_{-\mathbf{u}}, \mathbf{r}^i_{-\mathbf{u}}, \mathbf{m}^i_{-\mathbf{u}}, \mathbf{d_u}\big)$, which also increases the computational demand. In our experience, the mode indicator $\boldsymbol{\kappa_u}$ appears to be far more important for the mixing and convergence rates in the Markov chain Monte Carlo algorithm. There are other sampling strategies such as a moving-window update (see de Figueiredo et al. (2017)) or considering a model where each vertical profile is treated independently of all other traces (Connolly and Hughes, 2016). Finally, an extension of Fjeldstad and Omre (2020) is to first generate an ensemble of realizations from $p\big(\boldsymbol{\kappa} \mid \mathbf{d}\big)$ by iteratively sampling $\boldsymbol{\kappa_u} \sim q\left(\boldsymbol{\kappa_u} \mid \boldsymbol{\kappa}^i_{-\mathbf{u}}, \mathbf{d_u}\right)$ and accepting each realization with probability $\min\left\{1, \frac{p\left(\mathbf{d_u}|\boldsymbol{\kappa_u}\right)}{p\left(\mathbf{d_u}|\boldsymbol{\kappa}^i_{\mathbf{u}}\right)} \times \frac{\widetilde{p}\left(\mathbf{d_u}|\boldsymbol{\kappa}^i_{\mathbf{u}}\right)}{\widetilde{p}\left(\mathbf{d_u}|\boldsymbol{\kappa_u}\right)}\right\}$ based on the current value $\boldsymbol{\kappa}^i_{\mathbf{u}}$. Afterwards, exact realizations from $p\big(\mathbf{r} \mid \mathbf{d}\big)$ and $p\big(\mathbf{m} \mid \mathbf{d}\big)$ are obtained since the Gaussian mixture prior pdfs defined in equations (11) and (13) are conjugate priors for a Gauss-linear likelihood model (Grana et al., 2017).

RESULTS FROM A NORWEGIAN SEA CASE STUDY

We demonstrate the proposed methodology on a Norwegian Sea gas discovery; see Avseth et al. (2016) for details. The 3D seismic data consist of broadband prestack time-migrated and normal-moveout-corrected gathers from a survey covering the target area. We condition on near- and far-angle prestack AVO data and invert for the three distinct lithology/fluid

classes: brine sandstone, gas sandstone and shale. Moreover, we include the porosity ϕ, the water saturation s_w, the clay volume/proportion c, and the elastic attributes $\log \rho V_P$ (log P-impedance) and $\log V_P/V_S$ (log Poisson ratio). The data cover a domain discretized onto a grid with $98 \times 75 \times 100 = 735,000$ cells. The observations are regularly sampled in the depth domain every 4 ms and cover a lateral domain of approximately 4900 m $\times$ 3750 m. Note that the dimension of the variable space, being the number of spatially coupled univariate posterior pdfs to assess, is $6 \times 735,000 = 4,410,000$, and the dimension of the data space is $2 \times 735,000 = 1,470,000$. The domain contains one well, which we use for blind well validation.

Figure 2 displays the near- and far-angle prestack seismic AVO data for a 2D section containing the blind well. We observe the seismic AVO measurements to have a fairly long ranged horizontal spatial dependency. In Figure **??**, we display the variables of interest observed in the blind well together with the observed seismic signal and the set of synthetic seismic signals. We display spatial histograms of the continuous variables of interest and observe the variables to appear as either unimodal, multimodal or skewed due to varying lithology effects. The well-tie between the observed seismic and synthetic seismic signal, based on the likelihood parameters specified below, is reasonable. The corresponding correlations are 0.70 and 0.89 for the near and far angles, respectively. In Figure 4, we display the near- and far-angle wavelets. The signal-to-noise ratio is set to 2.5 for the near stack and 1.5 for the far stack, where most of the colored noise depends on the convolutional

model.

The prior model parameters defined earlier are empirically calibrated based on a well outside the target area. Figure 4 displays a subset of the empirically calibrated rock physics model: $\log \rho V_P$ against porosity and lithology/fluid class for a fixed value of water saturation and clay volume in logit($\mathbf{r}$) and $\mathbf{r}$ domain. The rock physics model is assumed to be a Gauss-linear model dependent on both the petrophysical properties and the lithology/fluid class in the logit($\mathbf{r}$)-domain. Note that this implies a nonlinearity in $\mathbf{r}$-domain for each lithology/fluid class. We assume vertical squared exponential spatial correlation functions for the petrophysical properties and elastic properties, both having a range parameter equal to two. The marginal prior pdfs defined in equation (11) and equation (13) will be discussed later. The correlation of $\log \rho V_P$ and $\log V_P/V_S$ is set to 0.8, to -0.5 for porosity and water saturation, to -0.65 for porosity and clay volume, and to 0.65 for water saturation and clay volume. The prior Markov random field is specified such that the marginal probabilities are $(0.5, 0.15, 0.35)$ for shale, gas and brine, respectively, together with an anisotropic spatial interaction in the depth and horizontal directions. Finally, we set $\varrho_r = \varrho_m = 0.5$ in the simulation algorithm.

We compare the results based on the proposed methodology to the results based on a set of trace-independent models, with each vertical profile being independent of every other vertical profile. The lithology/fluid class prior model in this trace-independent model is

assumed to follow a vertical Markov chain downwards with transition matrix

$$\mathbf{P} = \begin{pmatrix} 0.7 & 0.1 & 0.2 \\ 0.2 & 0.7 & 0.1 \\ 0.3 & 0 & 0.7 \end{pmatrix}, \tag{16}$$

which has marginal distribution $(0.47, 0.16, 0.37)^{\intercal}$. This marginal distribution is comparable to the one of the Markov random field prior in the proposed model. All other model parametes are fixed to the same values as in the laterally connected Markov random field model case. We refer to the two models as the 3D model for the proposed spatially-coupled model and the 1D model for the trace-independent model. We initiated the Markov chain Monte Carlo algorithm by simulating one realization from the prior Markov chain which we used as the initial sample in every vertical profile. We generated $10,000$ approximately independent posterior realizations after thinning by selecting every tenth from a set of $100,000$ realizations for both models after a burn-period of $10,000$. Since our simulation algorithm is a block-Gibbs Markov chain Monte Carlo algorithm, where successive realizations are highly correlated, thinning is required to provide approximately independent posterior realizations. In Figure 5 we display convergence of the negative log-likelihood $\Big(-\log p\big(\mathbf{d} \mid \mathbf{m}\big)\Big)$ and the lithology/fluid class proportions based on the two models. We observe convergence within a few thousand iterations for the 3D model and a few hundred iterations for the 1D model. In Table 2 a summary of the average lithology/fluid class proportions are given. The 3D model is observed to predict a 5.9 percentage points higher gas proportion than the 1D model. For the 3D model, we obtain an average acceptance

rate of 27.8 % across all vertical traces (min. 6.3 % and max. 64.5 %); correspondingly, we obtain 14.2 % (min. 2.0 % and max. 69.5 %) for the 1D model. The trace-wise acceptance rate is dependent on the similarity of the proposal density in the simulation algorithm and the correct posterior model (Fjeldstad and Omre, 2020). On a 12-core shared university workstation from mid-2016, the computational requirement for the 3D model is 24 hours, and it is seven hours for the 1D model.

To validate and compare the two models, we display the resulting posterior pdfs for the variables of interest at the blind well location. Figure 6 contains the reference lithology/fluid classification together with a set of posterior realizations, the marginal posterior pdf for the lithology/fluid classes and the MMAP predictor for the lithology/fluid classes. Overall, the two models have similar marginal posterior characteristics; however, the 1D model fails to identify the thin top gas reservoir in the MMAP predictor. Additionally, the MMAP predictor based on the 3D model predicts the bottom gas zone to be thicker than that for the 1D model. Indeed, the thin shale-layers around depth 2450 ms are not identified in the MMAP predictors, which may not be surprising since predictions are known to be more homogeneous than in reality. Note that these shale layers appear in the posterior realizations. In summary, introducing a lateral spatial dependence into the probabilistic model appears to help to identify thin layers.

Figure 7 displays the posterior pdfs for the porosity, water saturation and clay volume for the two models at the blind well location. For each property, we display the log-prior pdf

together with the log-posterior models based on the 3D model and the 1D model to ease interpretation. The prior models for the petrophysical properties and elastic attributes need not be identical in the two models because of the different lateral coupling in the lithology/fluid class model, but we expect them to be very similar. For simplicity, we display the prior based on the 1D model. The marginal prior at each depth point for porosity is close to unimodal but skewed, while the marginal prior at each depth point is bimodal, with two modes close to zero and one for water saturation. In general, the MMAP predictors based on the 3D model and the 1D model are similar; however, the latter fails to capture the high-porosity zone and low-water-saturation zone around depth 2315 ms, where the top gas reservoir is located. The MMAP predictors are generally observed to be more homogeneous than the true profile. In general, we observe the posterior models based on the 3D model to have greater variability than those based on the 1D model, i.e., they have a larger pointwise uncertainty. Both models are able to satisfactorily capture the rapid transition from low to high water saturation at approximately 2360 ms, which corresponds to the boundary of the lower gas reservoir.

Figure 8 displays in a similar format as Figure 7 the posterior pdfs for $\log \rho V_P$ and $\log V_P/V_S$. We have included a depth trend in the prior for the elastic attributes with a higher expected response for $\log \rho V_P$ at the bottom of the target zone than on top. Again, we observe the 3D model to have a more realistic level of uncertainty compared to the observed well measurements. In Figure 9 we plot the synthetic seismic signals based on the

MMAP predictor for the 3D and 1D models together with the observed seismic signal and observe a reasonable match.

The marginal posterior pdfs need not be unimodal but rather may be both multimodal and skewed; see Figure 10. The pdfs in the figure are chosen at time depths to represent a variety of the posterior models, which are observed to be unimodal, skewed and multimodal. Note the large discrepancy between the posterior models at locations 2300 ms and 2324 ms, which corresponds to the top reservoir and the upper part of the lowermost reservoir at the blind well location. Note that the marginal modes for the posterior pdfs for the petrophysical properties and elastic attributes are strongly dependent on the corresponding marginal posterior pdf for the lithology/fluid classes, which acts as the weights in the Gaussian mixture model. We interpret the smaller marginal variances for the 1D model to be the result of a bias-variance trade-off, where we have obtained a smaller marginal variance at the cost of a biased predictor.

In Table 3, we present the mean absolute error (MAE) and root mean square error (RMSE) for the two models at the blind well location. Except for the clay volume, we obtain an improvement of up to 59 % for the MAE and 62 % for the RMSE for the variables of interest.

In Figure 11 through Figure 13, we display posterior results for the 2D section corresponding to the seismic data presented in Figure 2. In Figure 11, the marginal probabilities for the three lithology/fluid classes and the corresponding MMAP predictor for the two

models are presented. In general, the marginal posterior characteristics are observed to be similar; however, the lateral connectivity is larger for the 3D model. Since the MMAP predictor is a marginal property, the lateral connectivity does not need to be preserved in the predictor. Figures 12 and 13 display the MMAP predictor for the petrophysical properties and elastic attributes, respectively. For the 3D model, we observe the gas zones to be thicker and the predictions to be more homogeneous.

The MMAP predictor for the lithology/fluid classes based on the 3D model appears too blocky around a depth of 2350 ms in Figure 11, which is not necessarily in correspondence with the observed seismic in Figure 2. In Figure 14 we display near angle synthetic seismic based on the MMAP predictor for the elastic attributes for both models, and compare them with the observed seismic. We observe the synthetic seismic sections to share the main characteristics of the observed seismic data, but the synthetic seismic sections appears as more spatially smooth. The latter is as expected since the synthetic seismic sections are generated based on the MMAP predictions. Similar results are observed for the far angle seismic, but the results are not included here. Note that the abovementioned thin shale layer appears to be present in most of the posterior realizations, not displayed here, but its shape and depth location varies due to the uncertainty. Therefore the thin shale layer does not appear in the MMAP predictor since the predictor is an aggregate over the posterior realizations.

Next, we present the results for the variables of interest in a three-dimensional view

based on the two models. In Figure 15, we present the MMAP predictor for the lithology/fluid classes based on the two different models. In general, we observe the MMAP predictor based on the 3D model to have a larger spatial connectivity in the lateral directions, as expected. The main characteristics of the sand bodies are observed in both models, but the MMAP predictor based on the 1D model appears to be less smooth and include abrupt invalid geophysical transitions. One advantage of the more complex 3D model is that each posterior realization appears with stronger spatial connectivity, which resembles more geologically plausible scenarios such as elongated sand bodies and channels that allow fluid flow (Figure 16). In Figure 17, we display the ISO-50 cube for gas (more than 50 % probability of gas) based on the two models. The 3D model is observed to have a far greater lateral extent of the gas reservoir, while the 1D model is observed to have less connectivity. A similar conclusion is drawn from Figure 18, where we display a set of horizontal slices for the marginal probability of gas for three consecutive horizontal layers. The main characteristics are shared across the two different models; however, the marginal probabilities based on the 3D model appear smoother, as expected. Note that the marginal probabilities are smooth across the time slices.

In Figure 19 and Figure 20, we display the MMAP predictor for the petrophysical properties and elastic attributes in a 3D perspective based on the two models. They share the main characteristics, but the predictors based on the 3D model appear more laterally connected and smoother than those based on the 1D model.

DISCUSSION

We have evaluated the proposed model using a real 3D case study and compared it with a model consisting of a set of 1D models without spatial lateral dependency. We have proposed a spatially coupled Bayesian model to promote spatial continuity in the three-dimensional posterior realizations of the lithology/fluid classes, petrophysical properties and elastic attributes. This spatial continuity need not be present if each three-dimensional posterior realization is based on the set of vertical trace-independent inversions. The MMAP predictors will usually appear as smoother for both the 1D and 3D model since the seismic data is laterally smoothed during the pre-processing. The marginal posterior densities for the continuous-valued properties capture multimodality and skewness, a property observed in the well logs of the blind well. The mean square error predictions in the blind well are reduced by at most 60 % by using the proposed 3D model compared to a set of 1D models.

The reason for including lateral dependency in the Bayesian model is to provide three-dimensional posterior realizations that are laterally continuous and to better identify thin horizontal layers. Since seismic images are processed images of the subsurface, where the vertical traces are migrated to match its neighboring traces by some criterion, seismic data are laterally continuous. Therefore, the 1D model will also provide posterior predictions that are laterally smooth. However, while the three-dimensional posterior predictions are smooth, the three-dimensional posterior realizations do not need to be laterally continuous for the 1D model. If each three-dimensional posterior realization is used as input in a fluid

flow simulator, lack of lateral continuity may be a problem: both large scale heterogeneity and small scale continuity of the reservoir properties must be representative to obtain unbiased flow predictions. The 3D model also increases the predictive power based on the neighboring traces, hence thin lateral layers will be more easily identified than in the 1D model. Therefore, we have proposed a model including lateral smoothness in the prior model.

In our experience, it is challenging to specify the model parameters in the Gibbs formulation in such a way that it does not become too dominant relative to the likelihood. Finally, the 3D model is less prone to misaligned vertical traces and/or misspecification of the likelihood model because it acts as a spatial smoother.

However, the computational demand for the 3D model is severe compared to that of the 1D model since each Markov chain Monte Carlo iteration requires a rerun of the reverse algorithm conditional on the current value of the neighboring traces. Higher memory usage is also required because larger parts of the 3D cube need to be stored in memory in each iteration. We note that the 1D model is easily computed in parallel, while the 3D model requires a larger computational overhead to be parallelized. In our experience, the 1D model is feasible on a regular laptop, while the 3D model requires a workstation or cluster to be feasible.

CONCLUSIONS

We propose a one-step block-Gibbs update scheme for joint probabilistic prediction of lithology/fluid classes, petrophysical properties and elastic attributes in three dimensions. The proposed methodology is demonstrated on seismic AVO data from a Norwegian Sea discovery and is validated at a blind well position. Realistic lateral spatial connectivity, representative of shallow marine reservoir sands, is obtained in both realizations and predictions for the variables of interest for the 3D model.Compared to a 1D model based on inverting the set of vertical profiles independently, we obtain an increased average acceptance rate in the simulation algorithm and a significant reduction in the mean absolute error and root mean square error at the blind well location.

Future research should include joint statistical inference of the model parameters in the Gibbs formulation together with the variable prediction to avoid oversmoothing.

ACKNOWLEDGMENTS

The authors acknowledge the Uncertainty in Reservoir Evaluation (URE) initiative at the Norwegian University of Science and Technology (NTNU) for funding this research and PGS for providing the seismic data set.

REFERENCES

Aki, K. and Richards, P. (1980). *Quantitative Seismology: Theory and Methods*. W. H. Freeman and Co., New York.

Aster, R., Thurber, C., and Borchers, B. (2005). *Parameter Estimation and Inverse Problems*. Number v. 1 in International Geophysics series. Elsevier Academic Press.

Avseth, P., Janke, A., and Horn, F. (2016). AVO inversion in exploration — Key learnings from a Norwegian Sea prospect. *The Leading Edge*, 35(5):405–414.

Avseth, P., Mukerji, T., and Mavko, G. (2005). *Quantitative Seismic Interpretation: Applying Rock Physics Tools to Reduce Interpretation Risk*. Cambridge University Press.

Bachrach, R. (2006). Joint estimation of porosity and saturation using stochastic rock-physics modeling. *Geophysics*, 71(5):O53–O63.

Besag, J. (1974). Spatial Interaction and the Statistical Analysis of Lattice Systems. *Journal of the Royal Statistical Society. Series B (Methodological)*, 36(2):pp. 192–236.

Bosch, M., Mukerji, T., and Gonzalez, E. F. (2010). Seismic inversion for reservoir properties combining statistical rock physics and geostatistics: A review. *Geophysics*, 75:75A165–75A176.

Buland, A. and Omre, H. (2003). Bayesian linearized AVO inversion. *Geophysics*, 68(1):185–198.

Connolly, P. A. and Hughes, M. J. (2016). Stochastic inversion by matching to large numbers of pseudo-wells. *Geophysics*, 81:M7–M22.

de Figueiredo, L. P., Grana, D., Roisenberg, M., and Rodrigues, B. B. (2019). Gaussian mixture markov chain monte carlo method for linear seismic inversion. *Geophysics*, 84(3):R463–R476.

de Figueiredo, L. P., Grana, D., Santos, M., Figueiredo, W., Roisenberg, M., and Neto, G. S. (2017). Bayesian seismic inversion based on rock-physics prior modeling for the joint estimation of acoustic impedance, porosity and lithofacies. *Journal of Computational Physics*, 336(C):128–142.

Doyen, P. (2007). *Seismic reservoir characterization: an earth modelling perspective*. Education tour series. EAGE publications.

Doyen, P. M. (1988). Porosity from seismic data: A geostatistical approach. *Geophysics*, 53(10):1263–1275.

Eidsvik, J., Mukerji, T., and Switzer, P. (2004). Estimation of Geological Attributes from a Well Log: An Application of Hidden Markov Chains. *Mathematical Geology*, 36(3):379–397.

Fjeldstad, T. and Grana, D. (2018). Joint probabilistic petrophysics-seismic inversion based on gaussian mixture and markov chain prior models. *Geophysics*, 83(1):R31–R42.

Fjeldstad, T. and Omre, H. (2020). Bayesian inversion of convolved hidden markov models with applications in reservoir prediction. *IEEE Transactions on Geoscience and Remote Sensing*, 58(3):1957–1968.

Gamerman, D. and Lopes, H. (2006). *Markov Chain Monte Carlo: Stochastic Simulation for Bayesian Inference, Second Edition*. Chapman & Hall/CRC Texts in Statistical Science. Taylor & Francis.

Grana, D. (2016). Bayesian linearized rock-physics inversion. *Geophysics*, 81:D625–D641.

Grana, D. and Della Rossa, E. (2010). Probabilistic petrophysical-properties estimation integrating statistical rock physics with seismic inversion. *Geophysics*, 75:O21–O37.

Grana, D., Fjeldstad, T., and Omre, H. (2017). Bayesian Gaussian Mixture Linear Inversion for Geophysical Inverse Problems. *Mathematical Geosciences*, 49(4):493–515.

Gunning, J. and Glinsky, M. E. (2007). Detection of reservoir quality using Bayesian seismic inversion. *Geophysics*, 72:R37–R49.

Gunning, J. and Sams, M. (2018). Joint facies and rock properties bayesian amplitude-versus-offset inversion using markov random fields. *Geophysical Prospecting*, 66(5):904–919.

Hastie, T., Tibshirani, R., and Friedman, J. (2009). *The Elements of Statistical Learning: Data mining, Inference, and Prediction*. Springer Series in Statistics. Springer, New York, 2nd edition.

Houck, R. T. (2002). Quantifying the uncertainty in an AVO interpretation. *Geophysics*, 67(1):117–125.

Jullum, M. and Kolbjørnsen, O. (2016). A Gaussian-based framework for local Bayesian inversion of geophysical data to rock properties. *Geophysics*, 81:R75–R87.

Kemper, M. and Gunning, J. (2014). Joint impedance and facies inversion – seismic inversion redefined. *First Break*, 32:89–95.

Krumbein, W. C. and Dacey, M. F. (1969). Markov chains and embedded Markov chains in geology. *Mathematical Geology*, 1:79–96.

Landrø, M. (2001). Discrimination between pressure and fluid saturation changes from time-lapse seismic data. *Geophysics*, 66(3):836–844.

Lia, O., Omre, H., Tjelmeland, H., Holden, L., and Egeland, T. (1997). Uncertainty in reservoir production forecasts. *AAPG Bulletin*, 81(5).

Mavko, G., Mukerji, T., and Dvorkin, J. (2009). *The Rock Physics Handbook*. Cambridge University Press, second edition.

Mukerji, T., Jørstad, A., Avseth, P., Mavko, G., and Granli, J. R. (2001). Mapping lithofacies and pore-fluid probabilities in a North Sea reservoir: Seismic inversions and statistical rock physics. *Geophysics*, 66:988–1001.

Reeves, R. and Pettitt, A. N. (2004). Efficient recursions for general factorisable models. *Biometrika*, 91:751–757.

Rimstad, K., Avseth, P., and Omre, H. (2012). Hierarchical bayesian lithology/fluid prediction: A north sea case study. *Geophysics*, 77(2):B69–B85.

Rimstad, K. and Omre, H. (2010). Impact of rock-physics depth trends and Markov random fields on hierarchical Bayesian lithology/fluid prediction. *Geophysics*, 75:R93–R108.

Rimstad, K. and Omre, H. (2013). Approximate posterior distributions for convolutional two-level hidden Markov models. *Computational Statistics & Data Analysis*, 58:187–200.

Sen, M. K. and Stoffa, P. L. (2013). *Global Optimization Methods in Geophysical Inversion*. Cambridge University Press.

Tarantola, A. (2005). *Inverse Problem Theory and Methods for Model Parameter Estimation*. Society for Industrial and Applied Mathematics.

Tjelmeland, H., Luo, X., and Fjeldstad, T. (2019). A bayesian model for lithology/fluid class prediction using a markov mesh prior fitted from a training image. *Geophysical Prospecting*, 67(3):609–623.

Ulvmoen, M. and Omre, H. (2010). Improved resolution in Baeysian lithology/fluid inversion from seismic prestack data and well observations: Part I - Methodology. *Geophysics*, 75:R21–R35.

LIST OF FIGURES

log-prior density for $\log \rho V_P$, (b) log-posterior density for $\log \rho V_P$ based on the 3D model, (c) log-posterior density for $\log \rho V_P$ based on the 1D model, (d) log-prior density for $\log V_P/V_S$, (e) log-posterior density for $\log V_P/V_S$ based on the 3D model, (f) log-posterior density for $\log V_P/V_S$ based on the 1D model. The well logs are given in solid black and the marginal mode of the log-densities are given in dotted red.

9 1D comparison of synthetic seismic observations and observed seismic for near and far angle: (a) observed near-angle AVO (solid black), synthetic near-angle AVO based on 3D model (dashed red), synthetic near-angle AVO based on 1D model (dot-dashed blue) and synthetic near-angle AVO based on well log (dotted green), and (b) observed far-angle AVO (solid black), synthetic far-angle AVO based on 3D model (dashed red), synthetic far-angle AVO based on 1D model (dot-dashed blue) and synthetic far-angle AVO based on well log (dotted green).

10 1D posterior marginal densities at the blind well location: (a) porosity at 2300 ms, (b) $\log \rho V_P$ at 2300 ms, (c) porosity at 2324 ms, (d) $\log \rho V_P$ at 2324 ms, (e) porosity at 2420 ms, (f) $\log \rho V_P$ at 2420 ms, (g) porosity at 2500 ms, and (h) $\log \rho V_P$ at 2500 ms. Prior density given in black, observed well measurement in dotted green, posterior density based on the 3D model in dashed red and posterior density based on the 1D model in dot-dashed blue.

11 2D posterior marginal probabilities for the lithology/fluid classes: (a) shale (3D model), (b) shale (1D model), (c) gas (3D model), (d) gas (1D model), (e) brine (3D model), (f) brine (1D model), (g) MMAP predictor (3D model), and (h) MMAP predictor (1D model).

12 2D posterior MMAP predictors for the petrophysical properties: (a) porosity (3D model), (b) porosity (1D model), (c) water saturation (3D model), (d) water saturation (1D model), (e) clay volume (3D model), and (f) clay volume (1D model).

13 2D posterior MMAP predictors for the elastic attributes: (a) $\log \rho V_P$ (3D model), (b) $\log \rho V_P$ (1D model), (c) $\log V_P/V_S$ (3D model), (d) $\log V_P/V_S$ (1D model).

14 2D near-angle observed seismic versus 2D near-angle synthetic seismic generated from MMAP predictor: (a) observed near-angle AVO, (b) synthetic near-angle AVO generated from MMAP predictor (3D model), (c) difference between observed and predicted AVO (3D model), (d) observed near-angle AVO, (e) synthetic near-angle AVO generated from MMAP predictor (1D model), (f) difference between observed and predicted AVO (1D model).

15 3D MMAP predictor for the lithology/fluid classes: (a) 3D model, and (b) 1D model.

16 3D independent posterior lithology/fluid class realizations for the lithology/fluid classes from: (a) 3D model, (b) 1D model, (c) 3D model, (d) 1D model, (e) 3D model, and (f) 1D model.

17 3D ISO-50 probability for gas: (a) 3D model, and (b) 1D model.

18 3D posterior marginal probability of gas based on: (a) 3D model at 2312 ms, (b) 1D model at 2312 ms, (c) 3D model at 2316 ms, (d) 1D model at 2316 ms, (e) 3D model

at 2320 ms, and (f) 1D model at 2320 ms.

19 3D posterior MMAP predictors for the petrophysical properties: (a) porosity (3D model), (b) porosity (1D model), (c) water saturation (3D model), (d) water saturation (1D model), (e) clay volume (3D model), and (f) clay volume (1D model).

20 2D posterior MMAP predictors for the elastic attributes: (a) $\log \rho V_P$ (3D model), (b) $\log \rho V_P$ (1D model), (c) $\log V_P/V_S$ (3D model), (d) $\log V_P/V_S$ (1D model).

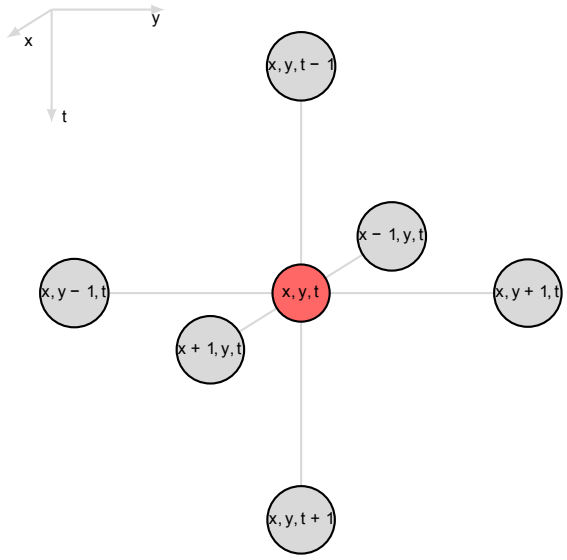

Figure 1: Stencil of neighborhood system. Current node $v = xyt$ marked in red and neighborhood system n_v in gray.

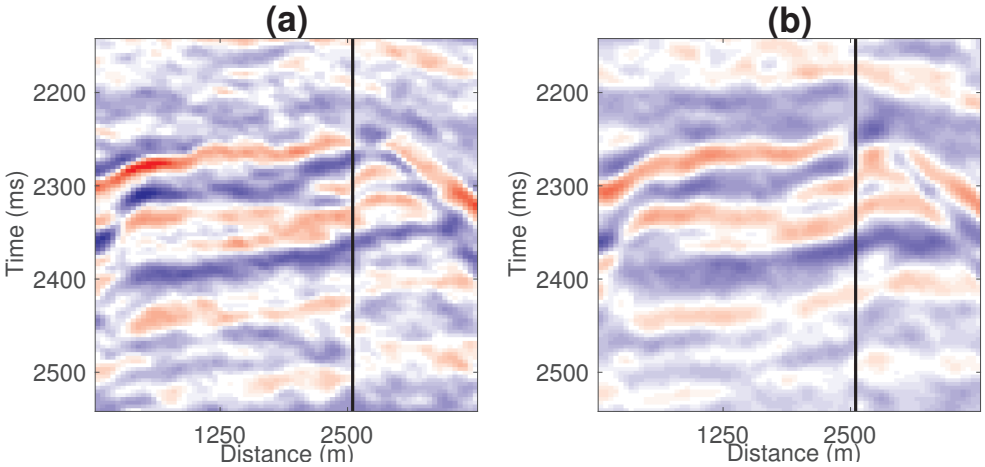

Figure 2: 2D vertical cross-section AVO observations: (a) near-angle AVO observations, and (b) far-angle AVO observations. Red indicates a positive amplitude (hard event) and blue indicates a negative amplitude (soft event). The location of the blind well is indicated by the solid vertical line.

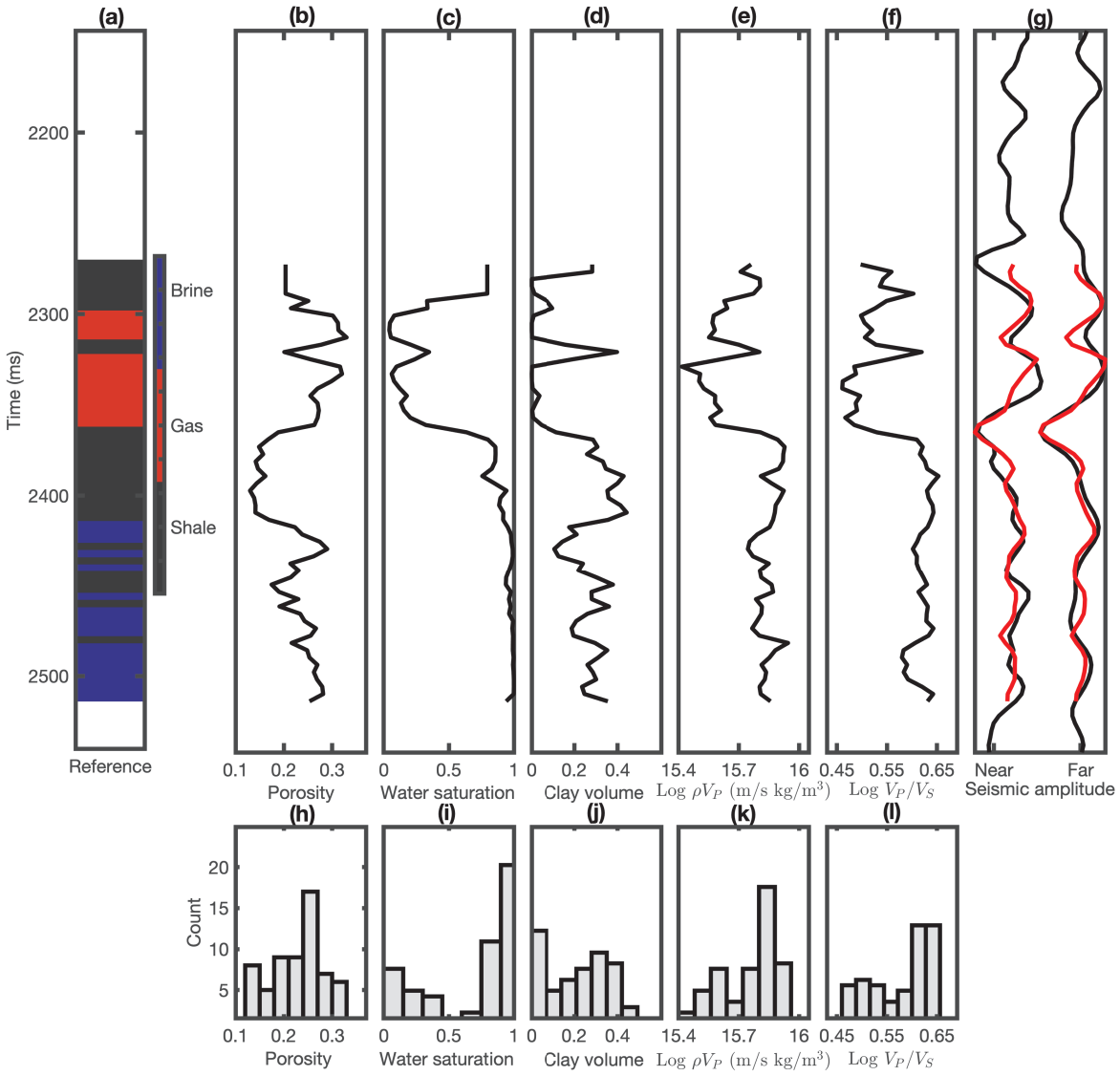

Figure 3: 1D blind well observations together with observed and synthetic seismic observations: (a) reference lithology/fluid classification, (b) observed porosity, (c) observed water saturation, (d) observed clay volume, (e) observed $\log \rho V_P$, (f) observed $\log V_P/V_S$, (f) near- and far-angle observed AVO (black) and near- and far-angle synthetic AVO (red), (h) marginal density porosity, (i) marginal density water saturation, (j) marginal density clay volume, (k) marginal density $\log \rho V_P$, and (l) marginal density $\log V_P/V_S$.

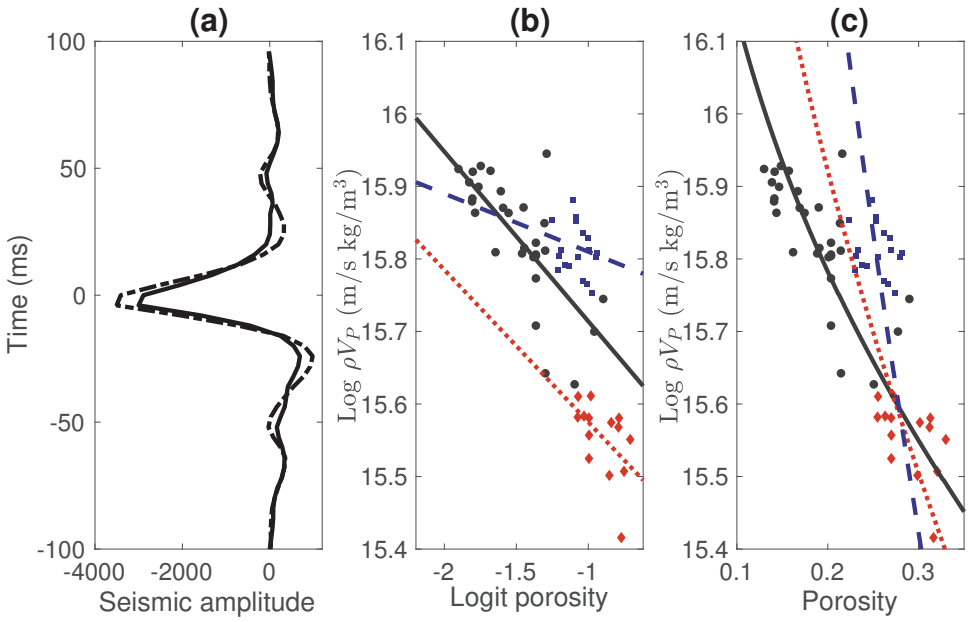

Figure 4: 1D wavelet and rock physics model: (a) near-angle (solid) and far-angle (dashed) wavelets, (b) $\log \rho V_P$ against logit-porosity and lithology/fluid class (shale in black, gas in red and brine in blue), and (c) $\log \rho V_P$ against porosity and lithology/fluid class (shale in black, gas in red and brine in blue).

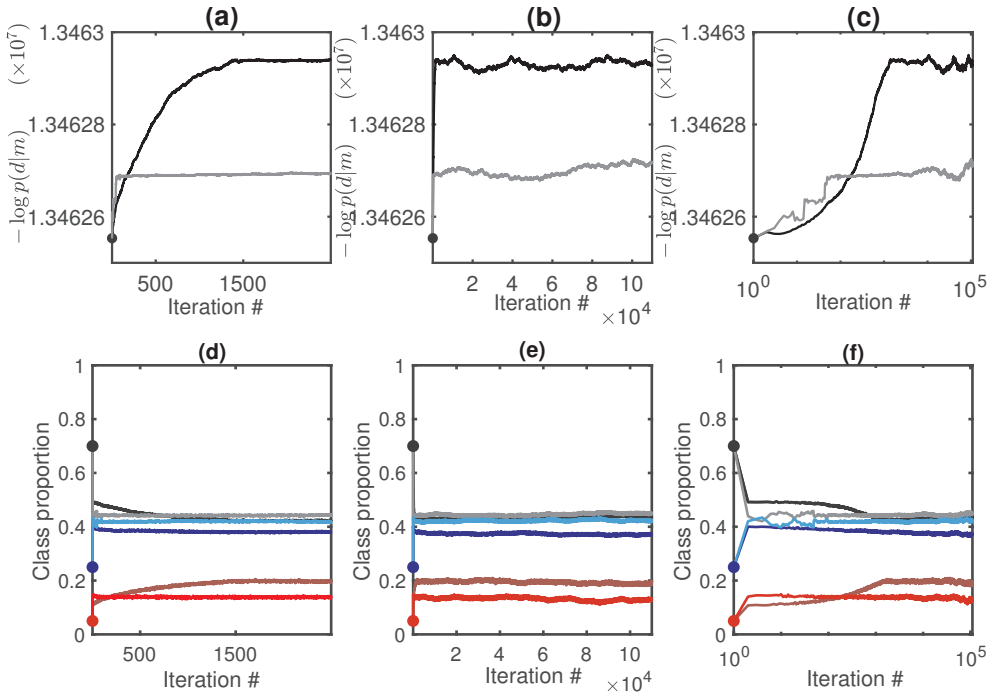

Figure 5: Convergence of negative log-likelihood and lithology/fluid class proportions: (a)-(c) convergence of the negative log-likelihood ($-\log p(\mathbf{d}|\mathbf{m})$ for the first 2,500 realizations (a), 110,000 realizations (b) and 110,000 realizations in $\log_{10}$-scale (c), and (d)-(f) convergence of class proportions for the first 2,500 (d), 110,000 realizations (e) and 110,000 realizations in $\log_{10}$-scale (f). Results based on the 3D model are displayed as lines in darker colors (black, dark red, dark blue) and results based on the 1D model are displayed in lighter colours (gray, light red, light blue).

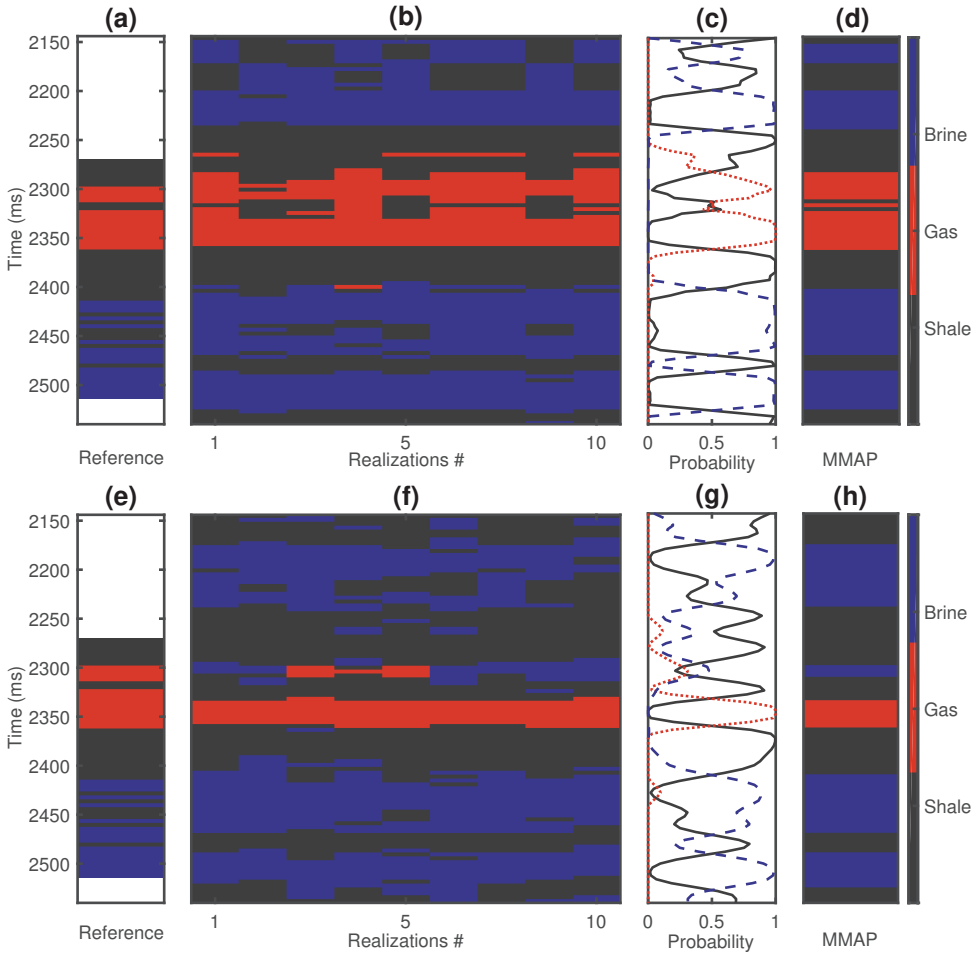

Figure 6: 1D posterior results lithology/fluid classes at the blind well location: (a) reference lithology/fluid class classification based on the blind well, (b) ten consecutive posterior realizations from the 3D model, (c) posterior marginal probabilities based on the 3D model, (d) MMAP predictor based on the 3D model, (e) reference classification based on the blind well, (f) ten consecutive posterior realizations from the 1D model, (g) posterior marginal probabilities based on the 1D model, (h) MMAP predictor based on the 1D model. Shale is displayed in black, gas in red and brine in blue.

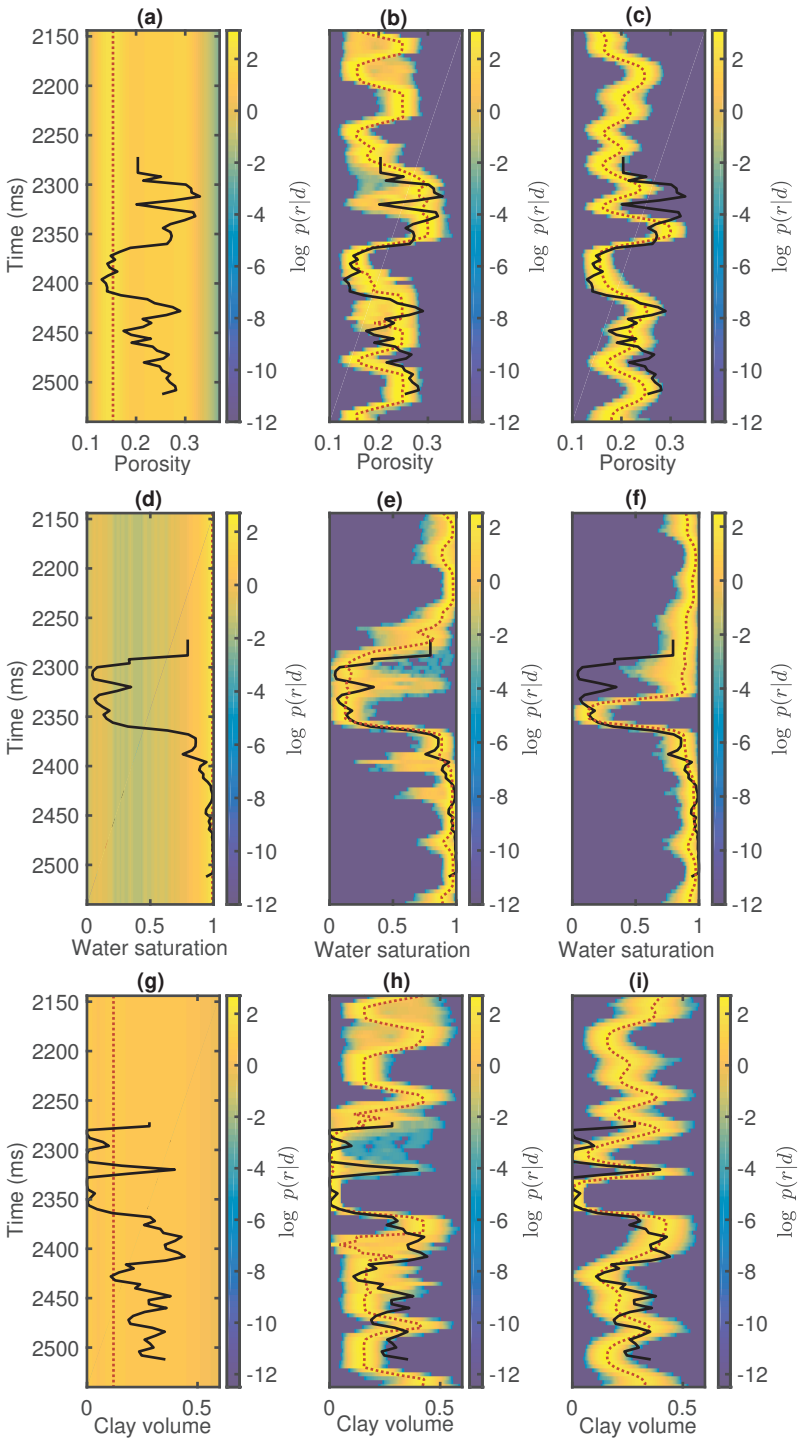

Figure 7: 1D posterior results petrophysical properties at the blind well location: (a) log-prior density for porosity, (b) log-posterior density for porosity based on the 3D model, (c) log-posterior density for porosity based on the 1D model, (d) log-prior density for water saturation, (e) log-posterior density for water saturation based on the 3D model, (f) log-posterior density for water saturation based on the 1D model, (g) log-prior density for clay volume, (h) log-posterior density for clay volume based on the 3D model, and (i) log-posterior density for clay volume based on the 1D model. The well logs are given in solid black and the marginal mode of the log-densities are given in dotted red.

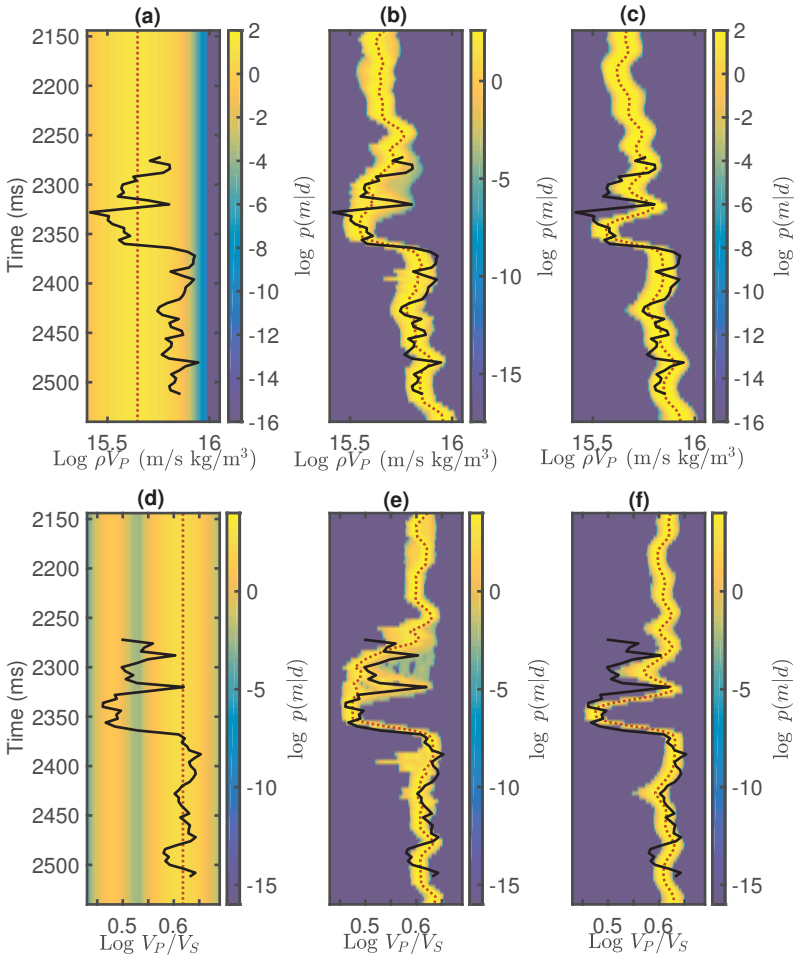

Figure 8: 1D posterior results petrophysical properties at the blind well location: (a) log-prior density for $\log \rho V_P$, (b) log-posterior density for $\log \rho V_P$ based on the 3D model, (c) log-posterior density for $\log \rho V_P$ based on the 1D model, (d) log-prior density for $\log V_P/V_S$, (e) log-posterior density for $\log V_P/V_S$ based on the 3D model, (f) log-posterior density for $\log V_P/V_S$ based on the 1D model. The well logs are given in solid black and the marginal mode of the log-densities are given in dotted red.

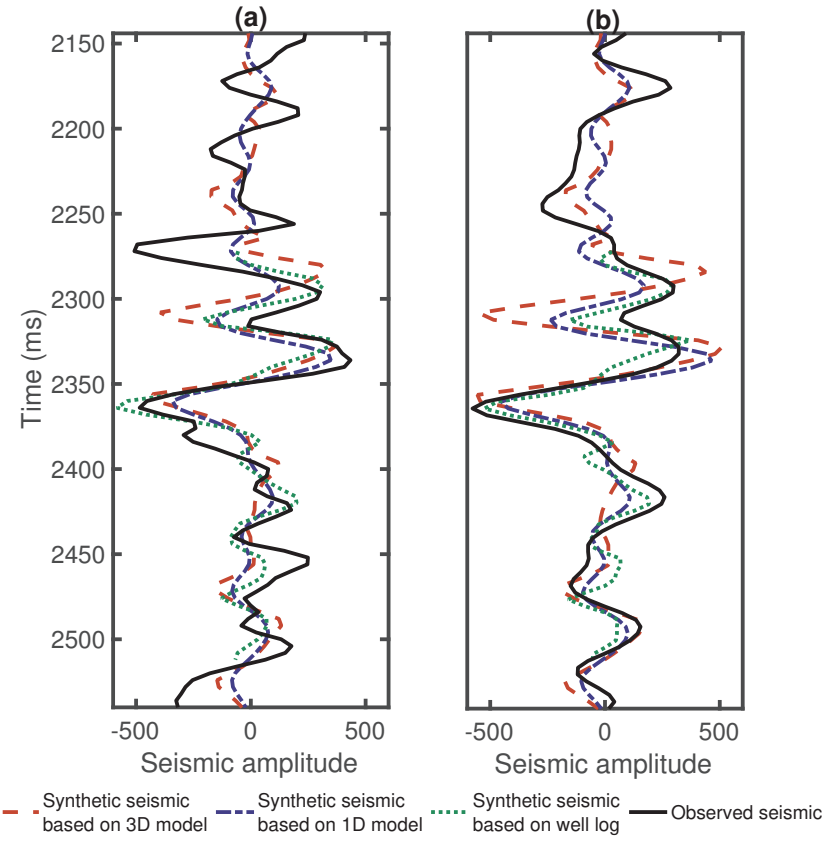

Figure 9: 1D comparison of synthetic seismic observations and observed seismic for near and far angle: (a) observed near-angle AVO (solid black), synthetic near-angle AVO based on 3D model (dashed red), synthetic near-angle AVO based on 1D model (dot-dashed blue) and synthetic near-angle AVO based on well log (dotted green), and (b) observed far-angle AVO (solid black), synthetic far-angle AVO based on 3D model (dashed red), synthetic far-angle AVO based on 1D model (dot-dashed blue) and synthetic far-angle AVO based on well log (dotted green).

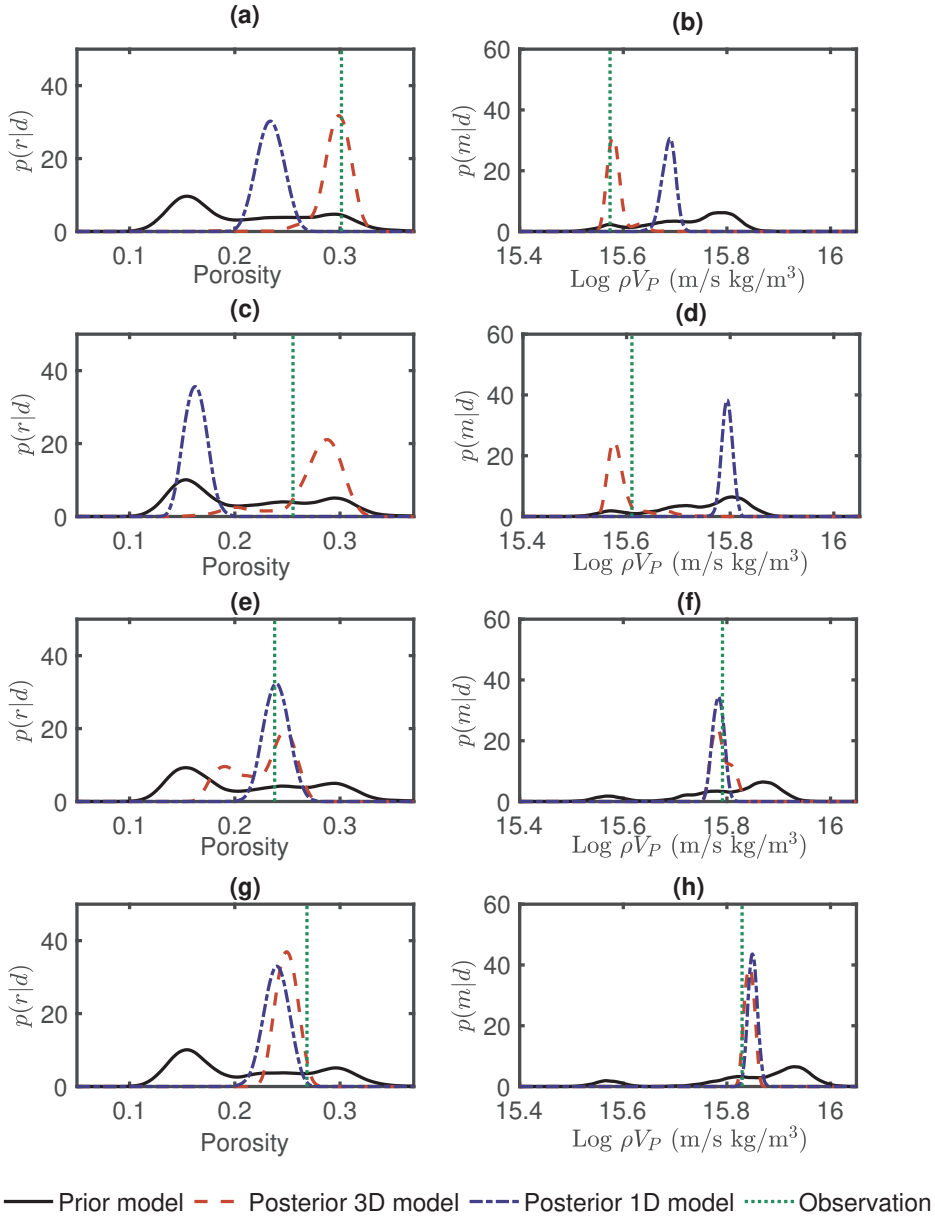

Figure 10: 1D posterior marginal densities at the blind well location: (a) porosity at 2300 ms, (b) $\log \rho V_P$ at 2300 ms, (c) porosity at 2324 ms, (d) $\log \rho V_P$ at 2324 ms, (e) porosity at 2420 ms, (f) $\log \rho V_P$ at 2420 ms, (g) porosity at 2500 ms, and (h) $\log \rho V_P$ at 2500 ms. Prior density given in black, observed well measurement in dotted green, posterior density based on the 3D model in dashed red and posterior density based on the 1D model in dot-dashed blue.

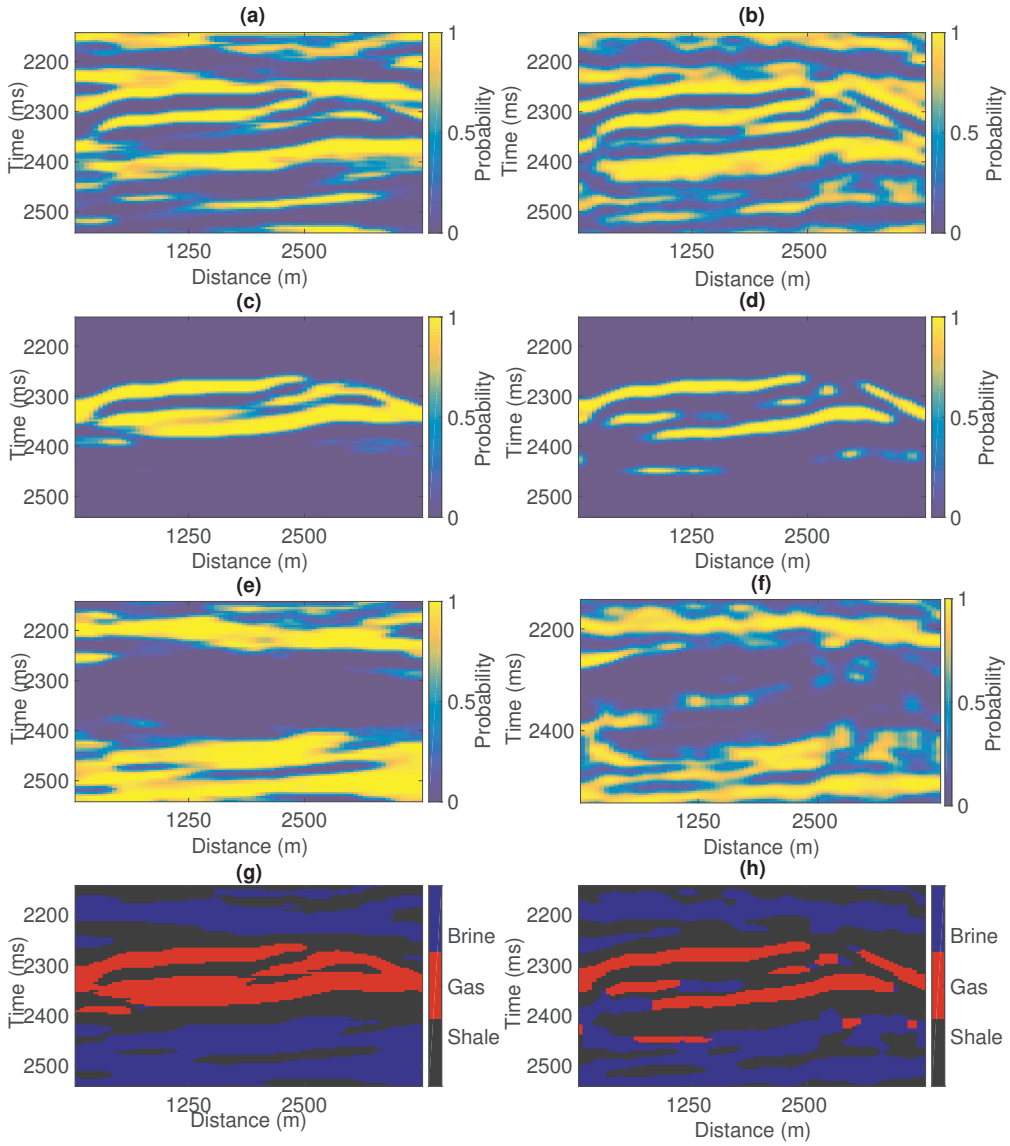

Figure 11: 2D posterior marginal probabilities for the lithology/fluid classes: (a) shale (3D model), (b) shale (1D model), (c) gas (3D model), (d) gas (1D model), (e) brine (3D model), (f) brine (1D model), (g) MMAP predictor (3D model), and (h) MMAP predictor (1D model).

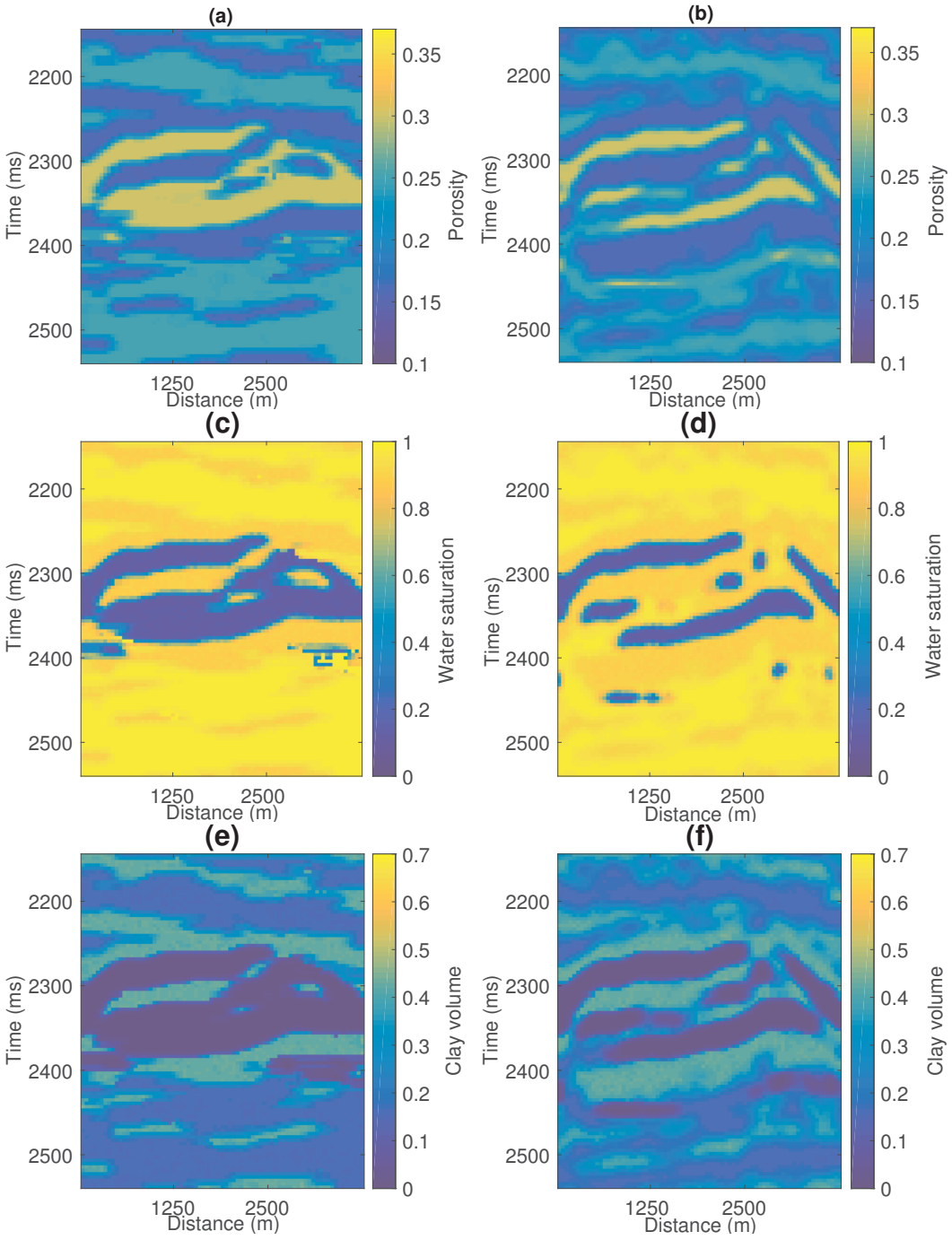

Figure 12: 2D posterior MMAP predictors for the petrophysical properties: (a) porosity (3D model), (b) porosity (1D model), (c) water saturation (3D model), (d) water saturation (1D model), (e) clay volume (3D model), and (f) clay volume (1D model).

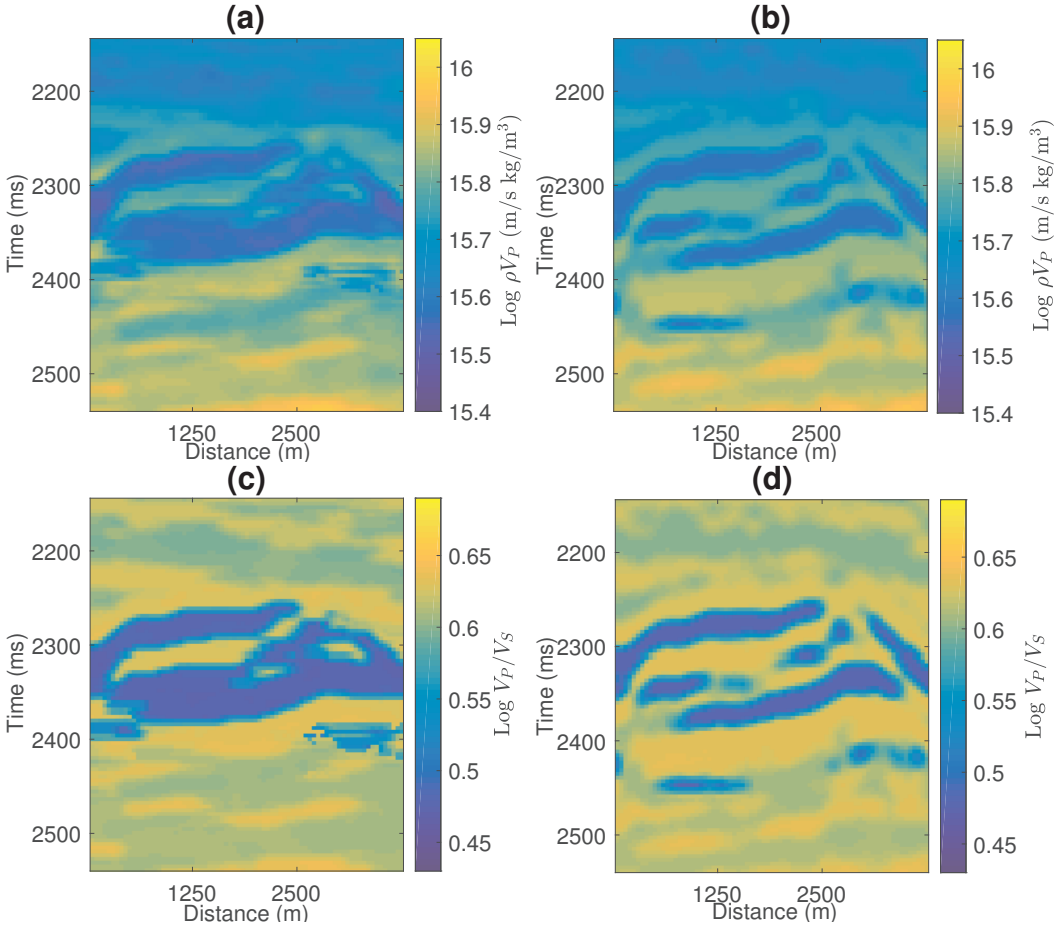

Figure 13: 2D posterior MMAP predictors for the elastic attributes: (a) $\log \rho V_P$ (3D model), (b) $\log \rho V_P$ (1D model), (c) $\log V_P/V_S$ (3D model), (d) $\log V_P/V_S$ (1D model).

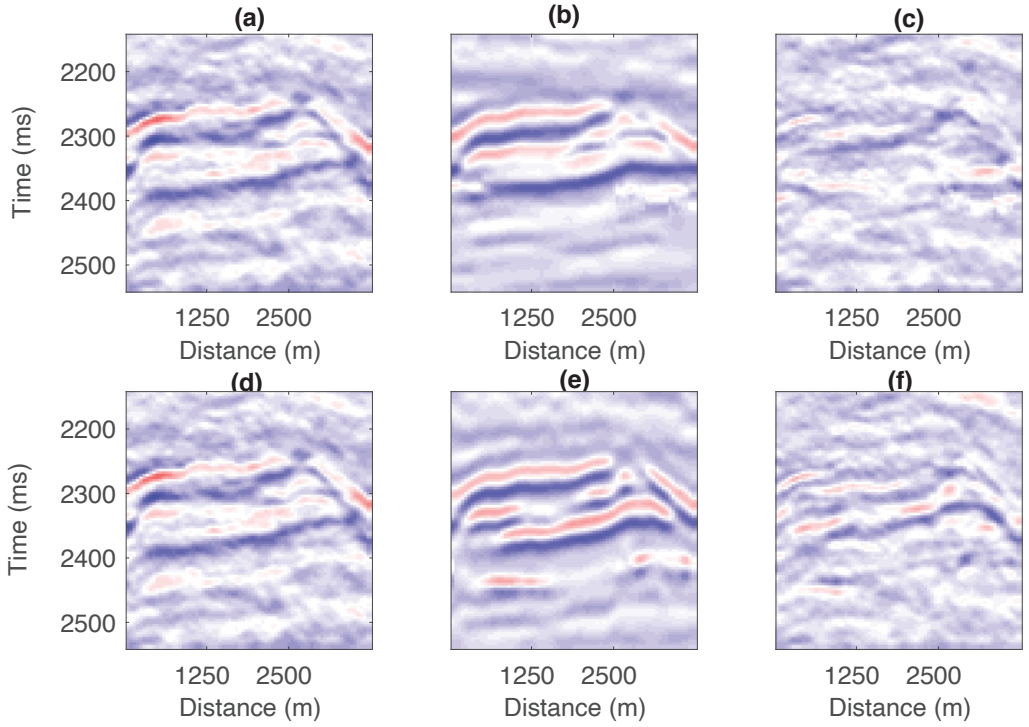

Figure 14: 2D near-angle observed seismic versus 2D near-angle synthetic seismic generated from MMAP predictor: (a) observed near-angle AVO, (b) synthetic near-angle AVO generated from MMAP predictor (3D model), (c) difference between observed and predicted AVO (3D model), (d) observed near-angle AVO, (e) synthetic near-angle AVO generated from MMAP predictor (1D model), (f) difference between observed and predicted AVO (1D model).

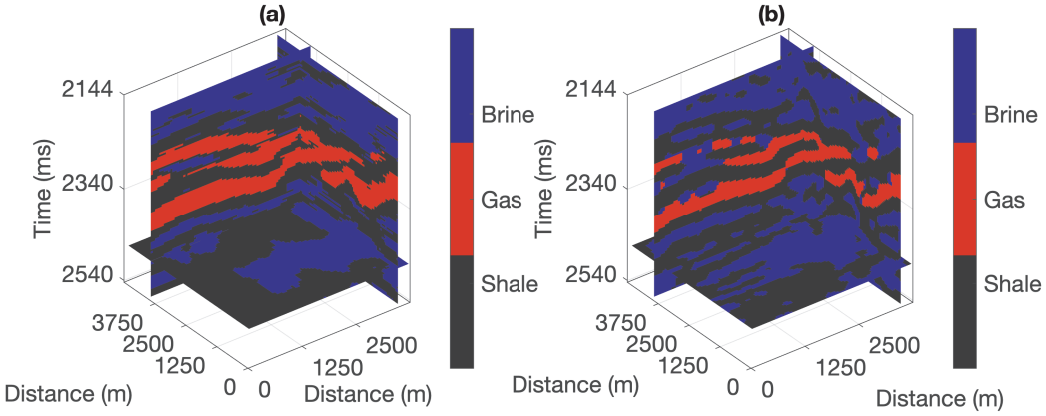

Figure 15: 3D MMAP predictor for the lithology/fluid classes: (a) 3D model, and (b) 1D model.

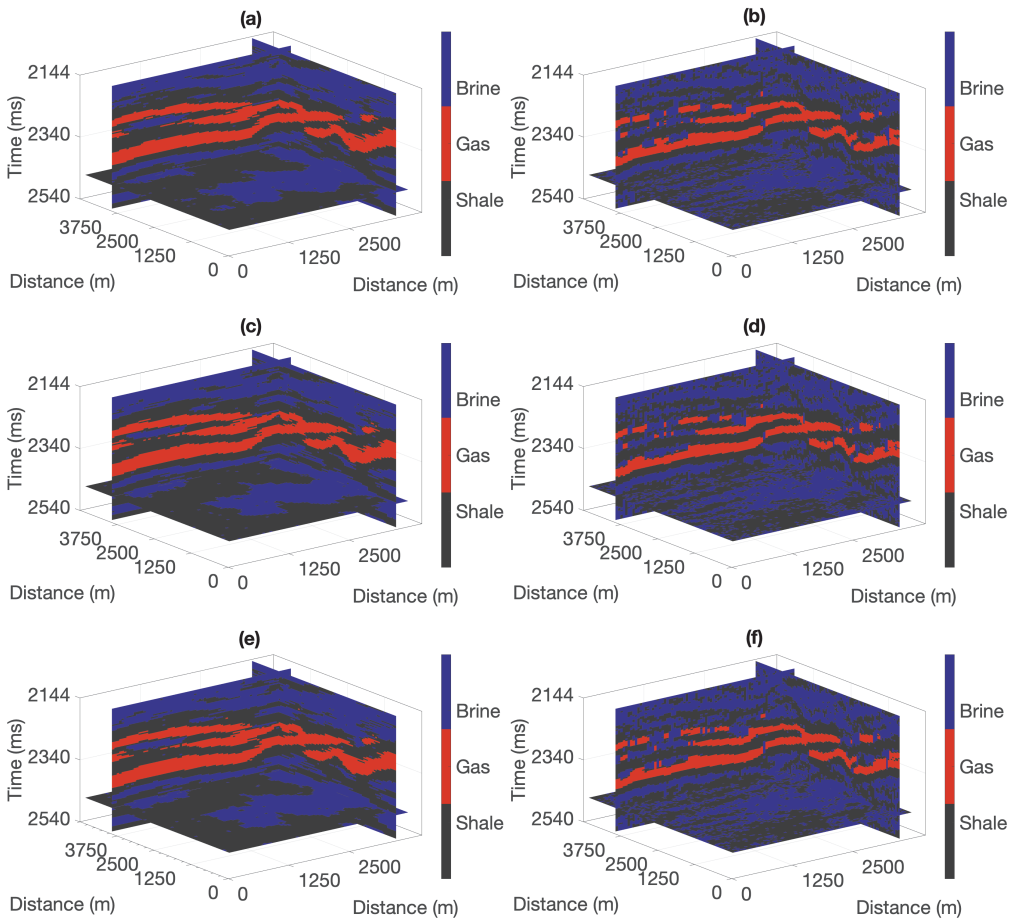

Figure 16: 3D independent posterior lithology/fluid class realizations for the lithology/fluid classes from: (a) 3D model, (b) 1D model, (c) 3D model, (d) 1D model, (e) 3D model, and (f) 1D model.

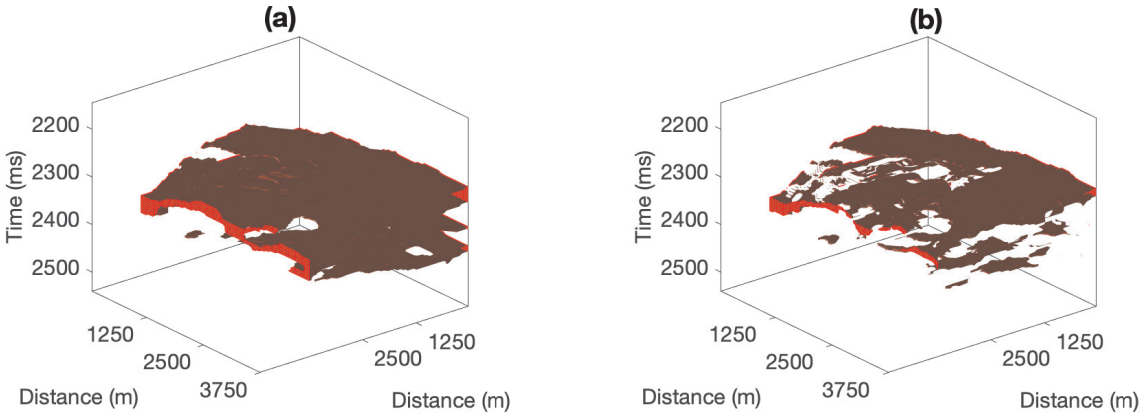

Figure 17: 3D ISO-50 probability for gas: (a) 3D model, and (b) 1D model.

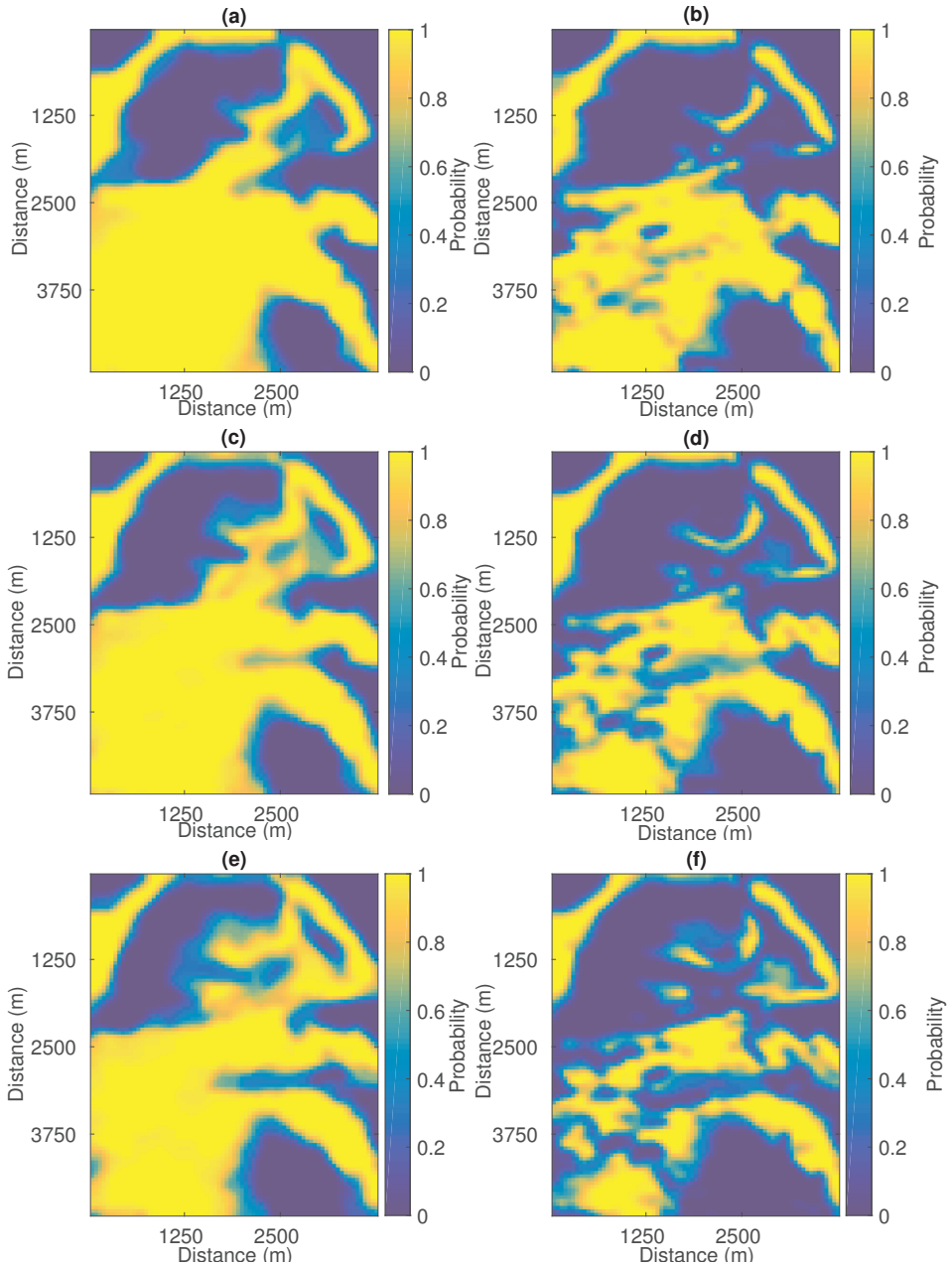

Figure 18: 3D posterior marginal probability of gas based on: (a) 3D model at 2312 ms, (b) 1D model at 2312 ms, (c) 3D model at 2316 ms, (d) 1D model at 2316 ms, (e) 3D model at 2320 ms, and (f) 1D model at 2320 ms.

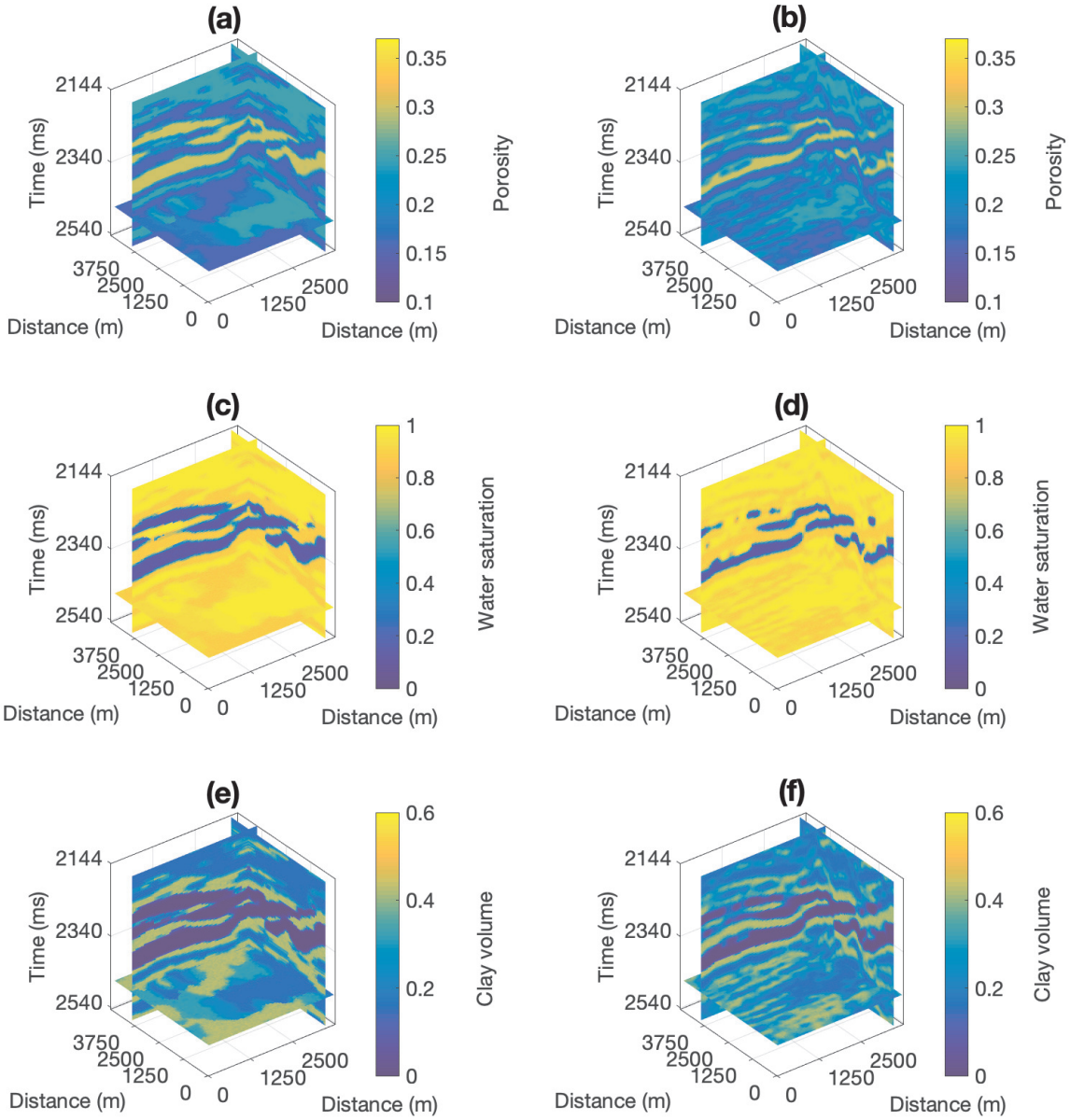

Figure 19: 3D posterior MMAP predictors for the petrophysical properties: (a) porosity (3D model), (b) porosity (1D model), (c) water saturation (3D model), (d) water saturation (1D model), (e) clay volume (3D model), and (f) clay volume (1D model).

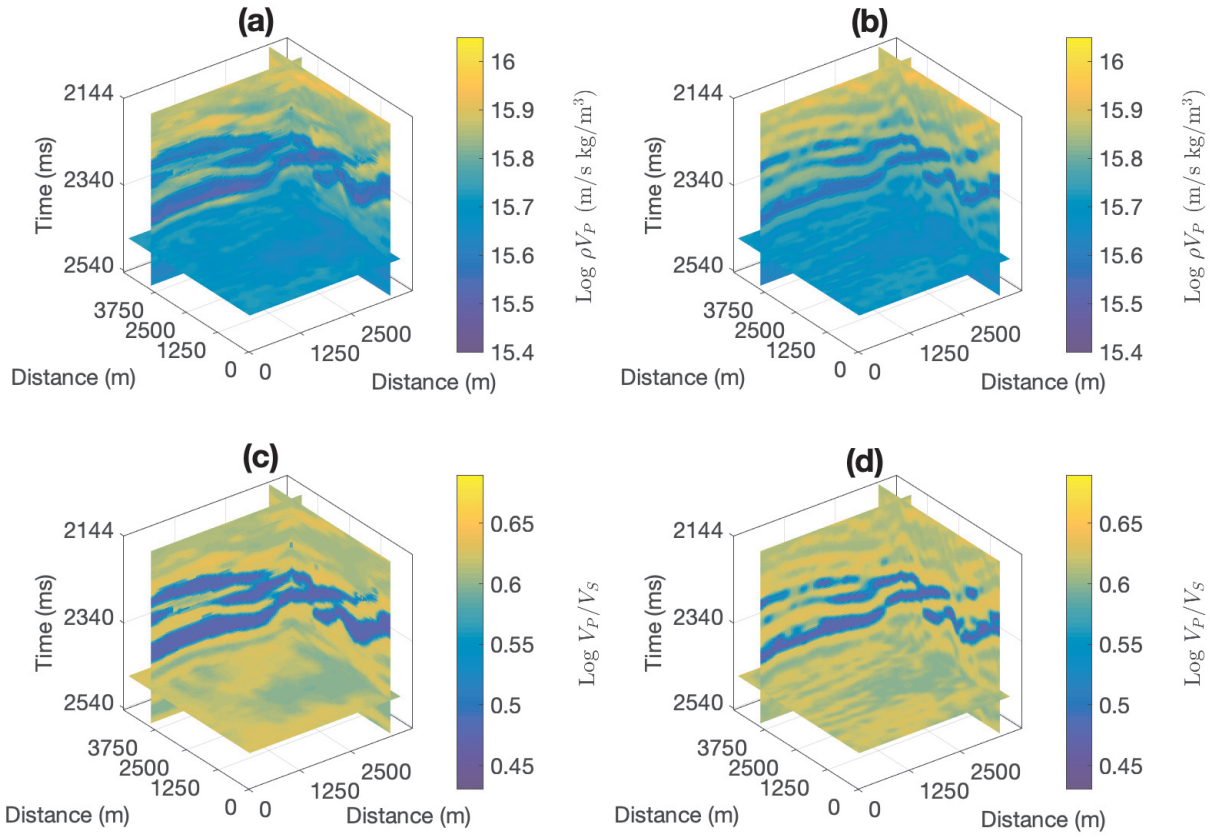

Figure 20: 2D posterior MMAP predictors for the elastic attributes: (a) $\log \rho V_P$ (3D model), (b) $\log \rho V_P$ (1D model), (c) $\log V_P/V_S$ (3D model), (d) $\log V_P/V_S$ (1D model).

LIST OF TABLES

Table 1: Overview of the variables to be defined.

Geophysical notation		**Grid-related variables**	
ϕ	Porosity	n_x, n_y	Number of vertical traces (horizontal)
s_w	Water saturation	n_t	Number of depth samples (vertical)
c	Clay volume/proportion	v	Grid cell ($v = (xyt)$)
ρV_P	Acoustic impedance	$\mathbf{u}$	Vector including indices of avertical trace ($\{(xyt) : t = 1, \ldots, n_t\}$)
V_P/V_S	Poisson ratio	$\mathcal{C}$	Clique system (set of all cliques)
		n_v	Neighborhood of a node v corresponding to $\mathcal{C}$
Variable	**Name**	**Associated parameter**	**Description**
$\boldsymbol{\kappa}$	Lithology/fluid classes	$\mathbf{P}$	Transition matrix
		$g_c(\cdot)$	Potential function wrt. cliques
		$h_v(\cdot)$	Potential function wrt. neighborhood system
$\mathbf{r}$	Petrophysical properties	$\boldsymbol{\mu}_{\mathbf{r_u}\|\boldsymbol{\kappa}_\mathbf{u}}$	Lithology/fluid dependent petrophysical properties trend
		$\boldsymbol{\Sigma}_{\mathbf{r_u}\|\boldsymbol{\kappa}_\mathbf{u}}$	Lithology/fluid dependent petrophysical properties covariance matrix
$\mathbf{m}$	Elastic attributes	$\boldsymbol{\mu}_{\mathbf{m_u}\|\boldsymbol{\kappa}_\mathbf{u}}$	Lithology/fluid dependent elastic attributes trend
		$\mathbf{B}_{\boldsymbol{\kappa}_\mathbf{u}}$	Matrix including lithology/fluid dependent rock physics model coefficients
		$\boldsymbol{\Sigma}_{\mathbf{m_u}}$	Lithology/fluid dependent elastic attributes covariance matrix
$\mathbf{d}$	Observations	$\mathbf{G}$	Linearized forward operator
		$\boldsymbol{\Sigma}_{\mathbf{d_u}}$	Likelihood covariance matrix
Statistical notation		**Simulation algorithm**	
$p(\mathbf{x})$	Probability density function of a random variable $\mathbf{x}$	$q(\cdot)$	Proposal density
$p(\mathbf{x} \mid \mathbf{y})$	Conditional probability density function of a random variable $\mathbf{x}$ given $\mathbf{y}$	ϱ_r, ϱ_m	Lateral coupling parameters for $\mathbf{r}$ and $\mathbf{m}$
$\mathcal{N}(\cdot)$	Gaussian probability density function	$\widetilde{p}(\cdot)$	Approximation based on Fjeldstad and Omre (2020)

Table 2: Average class proportion (%) for each of the three classes after convergence based on the two models. Initial proportion in parentheses.

Average class proportion (%)	**3D**	**1D**
Shale	43.5 (70.0)	45.3 (70.0)
Gas	19.1 (5.0)	13.2 (5.0)
Brine	37.4 (25.0)	41.5 (25.0)

Table 3: Mean absolute error and root mean square error for the petrophysical properties and elastic attributes for the two models at the blind well location.

	MAE		RMSE	
	3D	1D	3D	1D
Porosity	**0.0326**	0.0376	**0.0402**	0.0484
Water saturation	**0.0667**	0.1629	**0.1124**	0.2986
Clay volume	0.1014	**0.0819**	0.1353	**0.1130**
Log ρV_P	**0.0498**	0.0822	**0.0636**	0.0822
Log V_P/V_S	**0.0244**	0.0325	**0.0351**	0.0438